INVESTIGATING THE FEASIBILITY OF USING A POPULATION-BASED

INPUT FUNCTION FOR PHARMACOKINETIC MODELING OF [^{11}C]PBR28

DURING POSITRON EMISSION TOMOGRAPHY STUDIES IN A

POPULATION OF METHAMPHETAMINE USERS

By

Devin Schoen

A THESIS

Presented to the Medical Physics Graduate Program
and the Oregon Health & Science University
School of Medicine
in partial fulfillment of
the requirements for the degree of

Master of Science

June 2022

Table of Contents

List of Abbreviations

The following table describes the various abbreviations and acronyms used throughout this thesis. The page on which each is first used or defined is also given. The abbreviations for units commonly used in the field are not included for the sake of brevity.

Abbreviation	Meaning	Page
AUC	Area Under the Curve	30
BBB	Blood Brain Barrier	3
BMI	Body Mass Index	30
BP	Binding Potential	7
CBR	Central Benzodiazepine Receptor	9
C_F	Concentration of Free Tracer in Tissues	11
CM	Compartmental Modeling	16
C_{ND}	Concentration of Non-Displaceable Tracer	11
CNS	Central Nervous System	7
C_{NS}	Concentration of Non-Specifically Bound Tracer	11
C_{PET}	Concentration in Tissue on PET Scan	11
C_S	Concentration of Specifically Bound Tracer	11
CT	Computed Tomography	3
DA	Dopamine	22
FOV	Field of View	12
GA	Graphical Analysis	20
HPLC	High-Performance Liquid Chromatography	28
IDIF	Image-Derived Input Function	13
IF	Input Function	2
IR	Impulse Function	18
IV	Intravenous	25
LOR	Line of Response	5
LTI	Linear and Time-Invariant	18
MA	Methamphetamine	1

Acknowledgments

Foremost, I would like to thank the research team in Dr. Kohno's lab at the Portland VA, who made me feel welcome from day one of my work with them and did their best to get me any resources I needed. I was always excited to come into the lab because it gave me the opportunity to enjoy everyone's company.

To my mentor, Dr. Milky Kohno, I am sincerely grateful for your guiding hand in my project and my growth in the field. Your advice and encouragement have sparked excitement in me for pursuing a future in research and confidence in my ability to succeed in doing so.

I would also like to acknowledge Dr. Jeanne Link and Dr. Andrei Pugachev, both members of my advisory committee, who took the time when I first joined the program to understand my research interests and connect me with a project and supervisor who matched them.

My classmates have been a constant wellspring of comfort and joy through this program, and I feel so lucky to have spent two years alongside them. I am consistently inspired by their tenacity and creativity. I look forward to hearing about all the amazing success they find in their futures.

Last but not least, I could not have completed this thesis without the support and love of my mom, who supplied me with an empathetic ear and endless cups of late-night tea during my analysis and writing process.

Abstract

The innate neuroimmune response is characterized, in part, by proliferation and morphological changes of microglia and astrocytes. Over-activation of microglia results in the production of a number of pro-inflammatory markers and the release of reactive oxygen and nitrogen species that cause neuronal damage. Neuroinflammation can be quantified using position emission tomography (PET) to target upregulated peripheral benzodiazepine receptors (PBR) on activated microglia. Methamphetamine (MA) exposure leads to neurotoxicity and increases oxidative stress, inflammatory cytokine production, and gene and protein expression of factors associated with activated microglia. Despite clear evidence for the effects of MA on immunological pathways, the results using PET to quantify neuroinflammation in MA-use disorder have been mixed. This may, in part be attributed to different modeling methods and input functions (IF) being used across studies. Robust quantification relies upon pharmacokinetic modeling of the PET radiotracer using an IF to represent the compartment of available ligand. The gold standard for IF generation is the dynamic measurement of radioactivity within the plasma from arterial sampled blood. Arterial sampling, however, is invasive and can be difficult to perform in medically susceptible populations like intravenous drug users. An alternative to arterial sampling would substantially reduce patient burden and advance the scientific knowledge in vulnerable patient populations that present with neuroinflammation. Therefore, the aims of this thesis were to investigate if there is a significant difference in the tracer plasma concentrations between healthy controls (HC) and MA users and to identify an alternative to arterial Ifs by generating a population-based input functions (PBIF). Three quantification methods (compartmental modeling, spectral analysis, and graphical analysis) and two different scaling methods (blood activity-based and body mass index-based) were tested and compared. Arterial Ifs and PBIFs were generated using least-squares regression analyses. Through the application of statistical equivalency testing, no statistical differences between the concentration of activity within plasma were found between MA users and HCs, with all subjects falling within the equivalency bounds. Body mass index (BMI) to scale PBIF resulted in a strong correlation between the volume of distribution (V_T) obtained using an arterial IF and the V_T obtained using a PBIF, with Pearson correlation coefficients of 0.8 with spectral analysis and >0.9 with compartmental modeling and Logan graphical analysis. These modeling and scaling combinations, however, did not meet statistically significant levels of agreement. Although this study was underpowered, these preliminary data suggest a trend towards strong correlations between V_T obtained using an arterial IF and V_T obtained using a scaled PBIF. Recruitment for this study is ongoing and with added data, future analyses may produce results showing clinical application of PBIFs as a suitable replacement for arterial IFs.

INTRODUCTION

A growing literature indicates that neuroinflammation contributes to a number of neuropsychiatric and neurodegenerative pathologies. In substance use disorders (SUD), neuroinflammatory conditions may contribute to the maintenance of addiction through compromise of signaling pathways leading to an increase of withdrawal symptoms and decision making deficits. As such, therapies targeting neuroinflammation to treat SUDs and improve rates of relapse are ongoing. Investigation of these therapies requires accurate quantification of ng

Of particular public health concern is the drug Methamphetamine (MA). MA is widely abused throughout the United States (US) with high rates of overdose and hospitalization[1]. Previous studies linking MA use and associated symptoms with neuroinflammation using PET imaging have produced mixed results[2-4]. These studies used radiotracers with critical shortcomings like high levels of binding to non-receptor sites and low brain penetrance. A new generation of tracers targeting neuroinflammation has been developed to overcome these problems.

This project utilized the second-generation radiotracer [^{11}C]PBR28 to study the scope and implications of neuroinflammation in individuals with a methamphetamine use disorder (MUD). The primary aim of the parent study is to identify whether neuroinflammation is associated with cognitive control, craving, resting-state functional connectivity, and ventral striatal activation during monetary incentive delay tasks. The second aim of the parent study is a clinical trial in the MUD group designed to determine if quantifiable reductions in neuroinflammation resulting from treatment with the anti-inflammatory drug, Ibudilast correlate with improvements in behavioral and neurobiological deficits. Ibudilast is pharmaceutical approved for the treatment of asthma and indicated for the treatment of conjunctivitis and hay fever in Japan. Additionally, Ibudilast has shown promising results in reducing cravings and the use of MA[5].

1

Comprehensive PET quantification requires system modeling in order to account for the complex chemical and physical interactions at molecular levels in the processes of interest. System modeling requires a knowledge of the concentration of radiotracer in the plasma that is available for diffusion and possible binding. Radiotracer concentration is typically estimated by measuring the radioactivity in arterial blood samples throughout the PET scan. The parent study of this thesis precludes MA subjects from undergoing arterial sampling due to its invasive nature and high rates of line failure, particularly in fragile populations with confounding medical conditions[6]. For this reason, a comprehensive analysis within this patient population is difficult with the currently available methods.

The aims of this thesis were to determine if there is a valid alternative to arterial sampling for the purpose of pharmacokinetic modeling. Many of the methods proposed in the past to replace arterial sampling are computationally expensive, require additional imaging, or are not appropriate for all cohorts and imaging studies. Therefore, the first aim of this thesis was to determine if a population-based input function (PBIF) could be used in place of an individual arterial input function (IF) to derive kinetic parameters of receptor uptake. In an attempt to address the fundamental biological questions of whether chronic MA use affects tracer concentration in the plasma compartment, the second aim of this thesis was to determine if significant differences in the plasma tracer concentration exist between the HCs and the MA users. We hypothesize that the small amount of increased binding of TSPO associated with MA use would not affect the overall plasma concentration significantly. Favorable outcomes from these two aims would support the application of a PBIF generated using the arterial data from HCs to modeling in MUD group.

BACKGROUND

PET is a minimally invasive biomedical imaging technique. Although it was first theorized in the late 19th century and first implemented in the 1950s, it did not become widely used in hospitals and healthcare centers until the 1990s. Advances in radiation detection technology and computational ability have enabled PET imaging to become a viable tool for basic science researchers and medical clinicians to do things like measure glucose metabolism for research and cancer diagnoses, identify neurotransmitter signaling pathways and receptor density, index markers of inflammation, and investigate blood flow.

Unlike computed tomography (CT) or magnetic resonance imaging (MRI), PET imaging can provide information at the molecular level by labeling compounds that mimic naturally occurring substrates with radioactive isotopes. These radiotracers can be introduced into the body through various routes, such as venous injection, inhalation, or digestion. Radiation detectors collect the emitted particles from the region of interest, and iterative back projection is used to form a 3-dimensional image of radiotracer location and density. As such, PET can enable the imaging of biochemical processes in-vivo to investigate abnormal and normal physiology.

PET imaging has been instrumental in neuroscience with any radiotracers having been developed whose lipophilicity enables them to cross the blood-brain barrier (BBB) and enter brain tissues. Spatial resolution in PET, however, is limited due to decay particle interactions and behavior, making PET one of the lowest resolution imaging modalities in common use. PET is also not capable of providing vital anatomic information and will almost always need accompanying CT or MR imaging for anatomic localization.

Despite these limitations, PET imaging has been seminal to the basic understanding of neurotransmitter signaling. In conjunction with functional MRI, PET imaging has provided mechanistic support for the molecular underpinnings of functional brain activation[7]. Application

of PET in neuropsychiatric conditions such as addictions has provided evidence of abnormalities in dopaminergic signaling in key pathways thought to promote addictive behaviors[4]. With the development of new tracers, identification of novel neuropathological conditions in the context of addiction has emerged and extends beyond neurochemical interactions.

2.1 PET Imaging Physics and Technology

Many naturally occurring isotopes undergo beta-plus (β^+) decay when their nuclei are unstable due to an excess concentration of protons. Protons undergo nuclear change to transform into a neutron and consequently release a positron (electron anti-particle) and an electron neutrino. The resultant daughter species is a new nucleus with the same number of nucleons but an atomic number that has been reduced by one. The emitted positron will travel a short distance, losing energy until it interacts with an electron. The positron-electron pair will undergo annihilation, resulting in two 511-keV gamma photons moving anti-parallel (180° +/- 0.25°) to each other[8].

PET systems are designed with a ring of scintillator crystals coupled to photodetectors surrounding the subject (Figure 1). When photons interact with the scintillator crystal, visible light is produced, which then travels through the crystal and enters the photodetector[9]. The photodetector converts this visible light into a measurable electronic signal. The scintillator's visible light response is proportional to the energy that the incoming particle loses in the interaction. Furthermore, the amplitude of the electronic signal is proportional to the light yield from the scintillator[10]. If the crystals are thick enough to stop the incoming particles entirely it is possible to measure the energy of those particles and establish energy windows in order to specifically detect the 511-KeV photons of interest, discriminating against background sources of radiation and Compton scattered photons. Two signals detected opposite each other within an

acceptable time frame are deemed a coincidence event. A line of response (LOR) is drawn

between the two involved detector elements. If enough LORs are constructed, the region of

photon origin can be isolated[9].
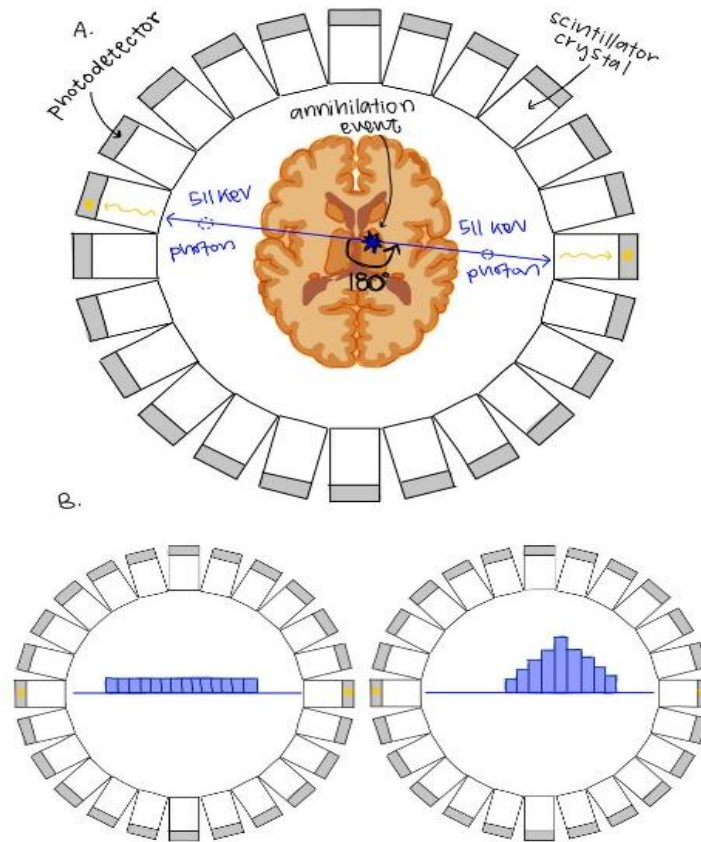
Figure 1: A. PET imaging takes advantage of matter-antimatter annihilation to localize the spatial distribution of a

radioactive tracer. At the source of annihilation, two photons are released in opposite directions. The photons will

be detected by the scintillator-photodetector complex if they lose energy. If two detector blocks pick up a signal

within the same time frame, a line-of-response (LOR) is drawn between them. If enough LORs are constructed,

localization of photon origin can be estimated. B. Time of flight (TOF) PET improves spatial localization by weighting

the LORs based on the time difference in signal detection between the two detector blocks involved and the known

speed of light.

      Dynamic PET imaging enables insight into temporal complexity of tracer dynamics and

can be used to investigate biological processes. Dynamic data acquisition is performed by

collecting frames of list data at set time intervals. Frames are reconstructed separately and form a time series representing the tracer distribution at distinct time points. Dynamic PET has had limited implementation in a clinical setting because of its added complexity, but is widely used in clinical and pre-clinical research studies[11].

Ideally, acquisition of PET images would be simultaneously collected with anatomical imaging in the form of a CT or MRI to reduce artifacts and distortions from subject movement. This is not always possible, depending on the resources available to researchers. The subject may need to be imaged on two separate scanners, and the images will undergo a transformation to be co-registered (figure 2). MRI is often the anatomical scan of choice for brain imaging studies because of its superior soft-tissue contrast. There are a number of software options that can perform registrations of images from PET and MR using both rigid (osseous) and deformable(grey matter/sulci) landmarks[12].
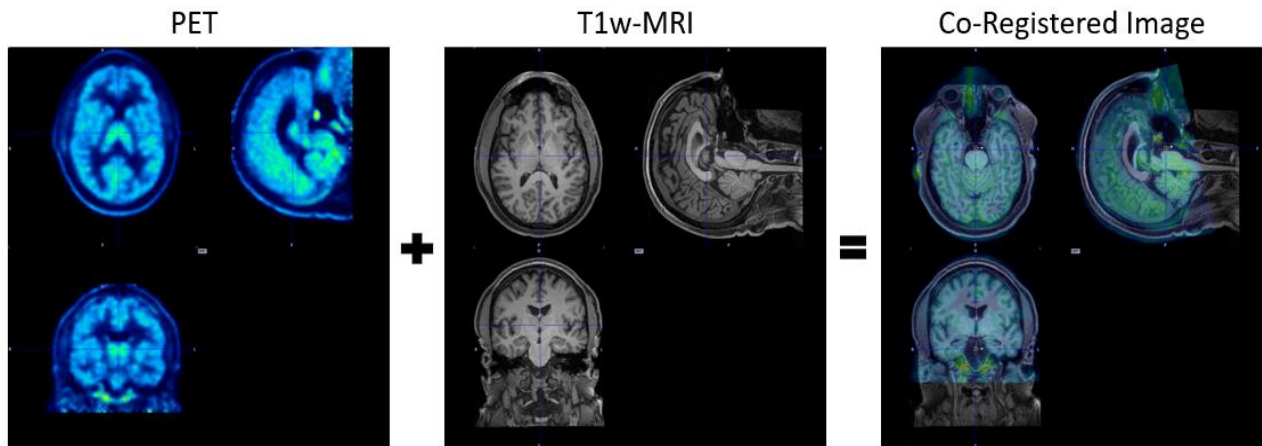
Figure 2: PET and MR images of the same study subject that were co-registered using Pmod^TM. Registration allows us to take advantage of the functional information of PET and the anatomical information of MRI congruently.

2.2 The Case for PET Quantification

Neurology and neuroscience studies often require quantification of slight changes in drug, hormone, or neurotransmitter uptake and concentration. The substances, known as ligands, will bind with receptor proteins to mediate chemical change between and within cells. Receptor

binding is a complex process that depends on plasma concentration, blood flow, tracer retention, and biological clearance. Dynamic PET acquisition paired with pharmacokinetic modeling describes how the injected substance will move and interact throughout the living. Each new radiotracer must undergo rigorous characterization before being used as a clinical quantification tool.

Complete pathophysiological quantitation is expensive both financially and computationally. It is also more difficult to find subjects and patients willing to undergo the long dynamic scan times and invasive procedures needed for complete kinetic modeling. For these reasons, total physiological quantitation is not often used clinically. Nevertheless, for the application of drug development and neuropsychiatric research studies, complete physiological modeling and quantitation is an invaluable tool.

Ligands are molecules that will bind with a receptor or other protein to serve some biological purpose. Ligand binding is a highly specific process with each receptor having an affinity for only one or a couple of ligands[13]. The rate of said binding will vary depending on the activation state of the receptor, which itself depends on varying physiological processes. As such, ligand binding is a standard imaging marker to identify receptor state, availability, and density.

In central nervous system (CNS) studies, receptor occupancy (RO) is used as a metric for blood barrier penetration, effectiveness of therapeutic pharmacodynamics, disease severity and abnormalities in receptor activation states. RO is defined as the relative change in a parameter at baseline and in a state of interest. The parameter most often used for RO calculation is Binding Potential (BP), but Volume of Distribution (V_T) is also commonly used. BP describes the

binding force of a receptor to its ligand. It is the product of the maximum density of a

neuroreceptor and the affinity of a specific receptor to the ligand[14].

$$RO = 100\% \times \frac{Baseline - State\ of\ Interest}{Baseline}$$ (1)

Accurate calculation of BP requires a reference region of tissue that exhibits no specific

tracer binding, such that any activity concentration detected by PET in this region will be due to

free and non-specifically bound tracer. Non-specific binding refers to when the radiotracer binds

to sites other than the targeted molecule. Many radioligands exhibit specific binding globally in

the brain, so defining such a reference region is often not possible. Although BP can be estimated

by non-linear estimation methods, the results of these estimations are highly dependent on image

noise and the initial guess of parameters[15]. V_T is often used to quantify receptor binding in these

situations because a reference region is not required for calculation[16]. V_T is the ratio of the

radioligand concentration in the tissue region of interest (ROI) to that in plasma at equilibrium,
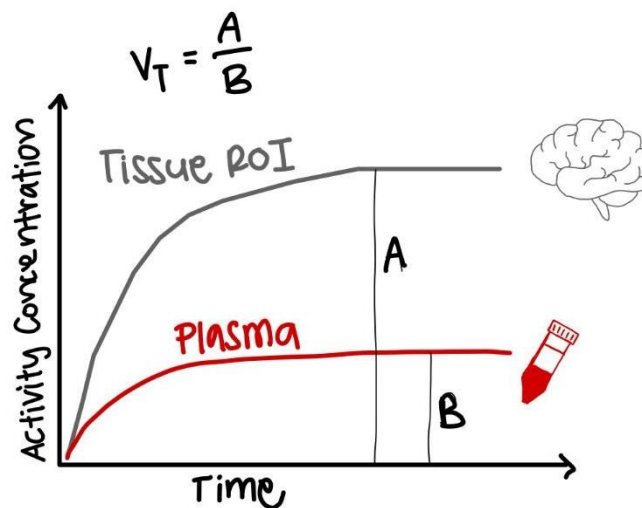
as depicted in figure 3.

Figure 3: Volume of distribution (V_T) represents the ratio of activity in tissue to the activity in plasma. V_T allows us to quantify how tracer is being concentrated in the tissues.

2.3 Nuclear Imaging of Neuroinflammation

Benzodiazepines are psychoactive drugs that bind to two structurally and pharmacologically distinct types of receptors: central benzodiazepine receptors (CBR) and 18kDa translocator proteins (TSPO), also known as peripheral benzodiazepine receptors (PBR)[19]. CBR is found exclusively in the CNS on the surface of neurons. In the CNS, TSPO is expressed on the surface membrane of mitochondria in glial cells like microglia and astrocytes. TSPO is also present in red blood cells and in peripheral tissues of the adrenal glands, heart, lungs, kidneys, and testes. TSPO is minimally expressed globally in the normal brain[17] but exhibits strong upregulation in microglia and astrocytes during pathological conditions. As TSPO can be globally expressed in brain, defining a true reference region devoid of receptor binding is difficult. An in vitro study suggests that TSPO is also expressed in neurons, which may further complicate possible interpretations of underlying biology[18]. However, these results have yet to be confirmed in-vivo. Another confounding factor is that TSPO is overexpressed in the endothelium of brain blood vessels[19]. The vascular fraction varies from person to person, with the endothelial TSPO binding fraction being less in aged brains and brains suffering from vascular fibrosis. Pharmacokinetic models accounting for this vascular binding contribution have been established and show improved accuracy and reproducibility[20]. These models, however, are not yet widely used in the field or implemented in common kinetic modeling software.

Within the CNS, TSPO is thought to regulate neurosteroid biosynthesis, mitochondrial function, and cellular proliferation[21]. The relationship between TSPO and neuroinflammation was not understood until an autoradiography and immunohistochemistry study demonstrated a correlation between elevated TSPO binding and the appearance of activated microglia[22]. Microglia are the immune cells of the CNS responsible for host defense and immune surveillance. Microglia are activated by pathological events in their environment, prompting

release of proinflammatory factors and toxins[23]. When microglia become activated, their TSPO

binding sites are upregulated to meet the increased mitochondrial energy burden. This link makes

TSPO binding a viable target for studying neuroinflammation in a variety of pathologies.

One of the first ligands designed to specifically bind to TSPO with high affinity was the

isoquinoline carboxamide derivative PK11195. In the 1990s and 2000s, [^{3}H]PK11195

autoradiography was used in studies exploring pathologies like multiple sclerosis, autoimmune

encephalitis, stroke, and traumatic brain injury[24]. As PK11195 suffers from low brain penetrance

and high levels of non-specific binding[25], second generation radioligands have been developed

including [^{11}C]PBR28, [^{18}F]DPA-714, [^{18}F]FEPPA, [^{11}C]DAA1106, and [^{18}F]PBR111. All of

these second-generation ligands have a much higher specific binding ratio (SBR) than PK11195.

While this is a major advantage over PK11195, limitations of the second-generation ligands

include high rates of vascular binding and increased intersubject variability in uptake. Most

significantly, within the TSPO encoding region of the human genome, a single nucleotide

polymorphism (rs6971) introduces variation in binding affinity for second-generation tracers[21]

This nucleotide substitution delineates between high-affinity binding sites and low-affinity

binding sites. To complicate matters further, rs6971 is a co-dominant gene meaning that

individuals' phenotypic expression can be characterized as (1) high-affinity binders (HAB), (2)

mixed-affinity binders (MAB), or (3) low-affinity binders (LAB). Differences in binding affinity

between the HAB, MAB, and LAB groups will depend on the specific ligand. Prior studies have

shown that binding of PK11195 is insensitive to TSPO phenotype[26,27]. The ligand PBR28

exhibits a large difference between groups, with HABs exhibiting approximately twice the

binding of TSPO as MABs. For this reason, all research subjects must undergo genetic

sequencing to stratify them into their binding affinity classifications, and many studies exclude individuals with LAB genetic status.

The synthesis method for PBR28 was first published in 2008[28]. This work highlighted the advantage of PBR28 to target TSPO by showing high SBR and superior brain penetrance. In addition, free fraction in the blood is simple to separate through chromatography due to in-vivo metabolism being limited to the production of just one polar radiometabolite. One of the carbon atoms making up the PBR28 molecule is replaced with ^{11}C. This isotope of carbon is radioactive, decaying with a half-life of 20.38 minutes[29] and can be easily produced in hospital-based cyclotrons. Due to the aforementioned favorable qualities of this radiotracer, this research aims to utilize PBR28 to validate and extend previous work that used first generation TSPO radiotracers to investigate MA-induced neuroinflammation[3].

2.4 Pharmacokinetic Modeling Inputs

Kinetic modeling of PET radiotracers requires two system inputs. One is arterial plasma concentration used to construct the IF, while the other is the time activity curve (TAC) in given ROIs from the PET data, $C_{PET}(t)$. Both of these are reported in units of activity per volume. $C_{PET}(t)$ contains the concentrations of (1) free tracer in the tissues ($C_F(t)$), (2) non-specifically bound tracer ($C_{NS}(t)$), and (3) specifically bound tracer ($C_S(t)$). $C_F(t)$ and $C_{NS}(t)$ will not change based on the pathology or drug treatments under investigation and can be combined into a single term called the non-displaceable concentration ($C_{ND}(t)$). For the current study and the pathophysiological question of interest, $C_S(t)$ will be modeled and mathematically expressed as:

$$C_S(t) = C_{PET}(t) - C_{ND}(t) \qquad\qquad (2)$$

The IF represents the amount of radioactive tracer available in the plasma compartment to penetrate the BBB and transfer into the non-displaceable tissue compartment. Arterial blood

sampling during PET imaging is the gold standard for IF generation. Though venous sampling is more comfortable for the subject and can be easier to set up and maintain than arterial sampling, venous plasma concentration is dependent on the sampling site due to differences in compound clearance in the vascular bed of different tissue types[30]. As such, the use of venous blood samples to construct IFs does not provide the requisite accuracy for PET studies. in contrast, the concentration of tracer in arterial plasma is independent of the sampling site[31].

Radiopharmaceuticals injected into the venous system travel to the heart and are subsequently dispersed systematically through the arterial system. A portion of the radiotracer molecules will attach to red blood cells and not be available to bind to receptors, while some of the radiotracer molecules will be taken up by organs, metabolized, and then re-enter the plasma[32]. However, lipophilicity of most of these metabolized compounds prevent BBB penetration and are therefore not available for receptor binding. In order to construct IFs for kinetic modeling, data on the quantity of the radiotracer in these three different states as a function of time are required. The IF is estimated through a combination of measurements and modeling methods based on known pharmacodynamics and the results of previous studies and will be detailed in the methods section.

Utilization of a reference region is the most commonly adopted alternative to arterial sampling for IF construction. A true reference region is a region that is devoid of any specific tracer binding. However, some tracers exhibit ubiquitous uptake in the organ of interest resulting in no suitable candidate regions to be used as a reference . Some studies using [^{11}C]PBR28 and other second generation TSPO radioligands have tested the use of pseudo reference regions for the implementation of pharmacokinetic modeling[33-35]. In a pseudo-reference region, there is

specific binding of the tracer, but the uptake amount is comparable between the study cohort and healthy controls (i.e. uptake in the region is not influenced by the pathology being studied).

In order to use a pseudo-reference region as a system input, prior studies are required to find regions that show no significant differences in quantitation between study groups for the specific radiotracer being used. Such studies have been performed for [^{11}C]PBR28 in Multiple Sclerosis and Alzheimer's Disease. At the time of writing this thesis, no similar efforts to find an appropriate pseudo-reference region have been reported for a population of subjects with MUD.

Another non-invasive alternative to arterial sampling is the use of an image-derived input function (IDIF). IDIFs can only be used with a small number of radiopharmaceuticals and still require blood sampling for validation, plasma corrections, and calibration. Creation of IDIFs require the field of view (FOV) of the PET acquisition to be expanded to include the cardiothoracic cavity or the ascending and descending aorta. Typically, TACs are reconstructed using PET data from one of these sources and is used as the IF. Many scanners do not have a FOV capable of simultaneously acquiring data from the neck and brain and would therefore require a separate bed position during the scan. This is particularly problematic for radiopharmaceuticals with short half-lives, where quickly decaying levels of activity would prevent adequate counts in both regions for reasonable statistics.

Several other issues must be addressed by groups attempting to use an IDIF to index neuroinflammation. First, inflammation of the arteries or heart can lead to an overestimation in the IDIF if receptors avidly take up the radiotracer in the inflammatory cells. This will lead to a higher IF than is physically accurate. In addition, the limited spatial resolution of 4-5 mm of PET imaging may lead to severe bias in the IDIF. As the diameter of the carotid artery is similar to the attainable resolution in PET, with an average internal carotid artery diameter of 5.11±0.87 mm

and 4.66±0.78 mm in men and women, respectively[36].Close proximity of arteries and veins may preclude differentiation of measurements from these sources using PET. This can lead to spillover and partial volume effects that cause inaccuracies using IDIF as a reference region. Zanotti-Fregonara et al.[37] investigated using an IDIF for [^{11}C]PBR28 imaging in a study of major depressive disorder and reported poor results and high variability depending on the quantification method and the radiometabolite fraction.

PBIFs are another alternative to arterial sampling. PBIFs are generated using data from many IFs obtained through arterial sampling that can be applied to an independent dataset of subjects without the need for invasive sampling. Intersubject variability is addressed by scaling the PBIF by various methods based on parameters like the injected dose or blood activity concentration at a single time point. The PET scan and reconstruction protocol must be highly standardized for this method to be accurate and reproducible.

A study using healthy non-human primates compared V_T obtained using an arterial IF, a PBIF, and a pseudo-reference region derived IF[38]. The PBIF was scaled in two different ways, one using the injected activity per body weight and one using the activity level in plasma from a single arterial blood sample. The study found the plasma activity scaled PBIF showed a strong correlation (r >0.90). But there was a poor correlation with their attempt to scale based upon injected activity per patient size(r = 0.46). The pseudo-reference region approach had the lowest correlation (r=0.26). Based on these and other promising results from studies implementing PBIFs[39-41], this was the method chosen as a candidate for replacing arterial blood sampling for subjects with MUD.

2.5 Quantification Methods

Standardized uptake volume (SUV) is a semi-quantitative method that is also referred to as the differential uptake ratio (DUR) or the differential absorption ratio (DAR) in literature. The simplicity of SUV has led to wide clinical use[42]. SUV is the ratio of the tissue radioactivity concentration (C_{PET}) measured in kBq per milliliter at time T and the injected dose divided by body weight measured in kBq per gram (equation 3). SUV is often treated as a dimensionless quantity because one milliliter of soft tissue is approximately one gram of soft tissue.
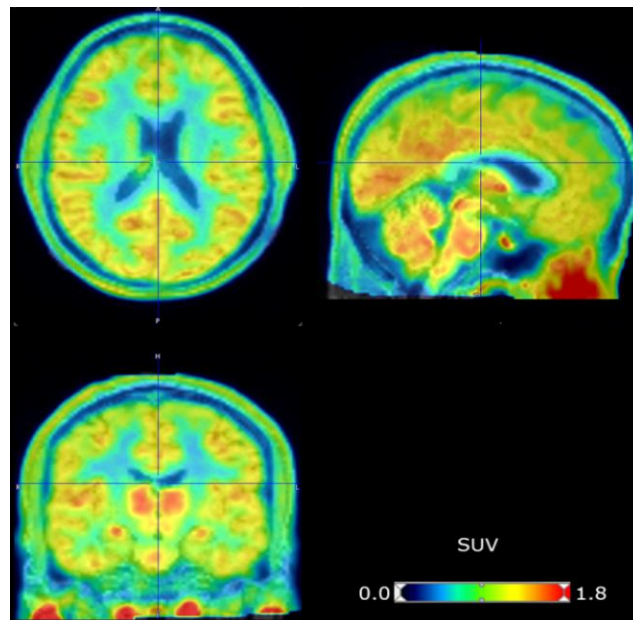

Figure 4: Standardized uptake volume (SUV) in one of our study participants. SUV can provide semi-quantitative information about the relative concentration of radiotracer in different regions, but does not take into account the entire biological system.

$$SUV = \frac{C_{PET}(T)}{Dose/Weight} \quad\quad (\,3\,)$$

As SUV does not consider any underlying pharmacodynamics, it does not quantify physiological processes such as receptor uptake. SUV has also been criticized because of its major sources of variability[43-45], including body composition and size, length of the uptake period, image noise, plasma glucose levels, and partial volume effects. Researchers have taken steps to address these variability issues by strictly standardizing protocols to limit the effects of

these confounding factors. SUV variability can be further reduced by taking the ratio of the SUV in the region of interest to the SUV in a reference region that shows minimal uptake. This is dubbed the SUV ratio (SUV_R). SUV remains clinically significant despite its shortcomings because it does not require blood sampling or complicated computational programming.

Full compartmental modeling (CM) is a kinetic quantification method that characterizes the fast tracer transfer between plasma, tissue, and receptors to estimate the rate constants and receptor density[14]. CM is widely accepted in the field as the gold standard for describing the underlying pharmacokinetics in PET experiments.
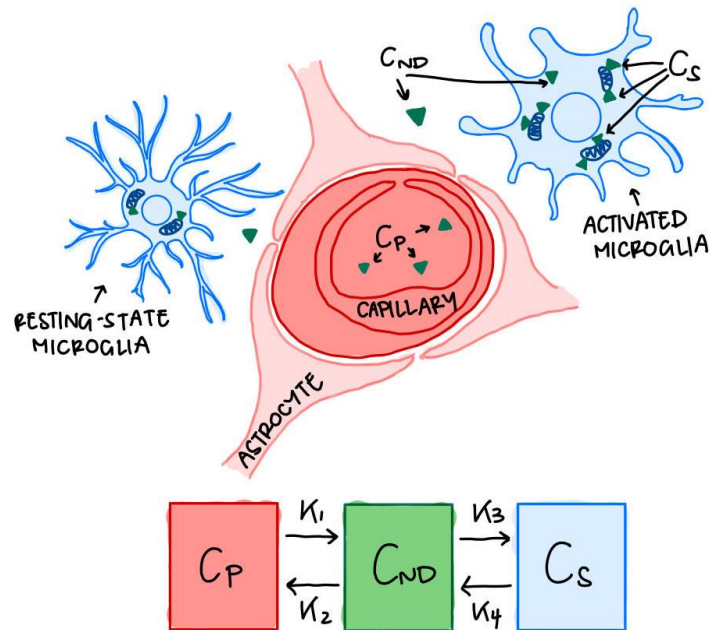

Figure 5: The radiotracer is injected intravenously and will travel within plasma around the body. When it reaches the brain, some amount of it will cross the blood-brain barrier, typically through passive diffusion. Once in the brain tissues, it can reside in a non-displaceable state, where pathology and intervention cannot affect the concentrations (free and non-specifically bound). It can also specifically bind to its receptor. These three states (plasma, non-displaceable, and specifically bound) are the compartments we use for our compartmental model. K_i are the transfer rates of tracer between these compartments.

A two-tissue compartmental model (2TCM) is the most commonly used compartment organization for [^{11}C]PBR28(Figure 5). Here, C_P is the concentration of radiotracer in the plasma compartment, and C_{ND} and C_S are two pharmacologically distinct compartments within the

tissue. Note that this does not necessarily mean two geographically distinct compartments. In this case, C_{ND} represents the concentration of non-displaceable radiotracer, and C_S represents the concentration of specifically bound radiotracer. K_1 and K2 are the rates at which the tracer diffuses into and out of tissues. K_3 and K_4 are the rates of binding and dissociation from TSPO receptors, respectively[46]. As the transfer rates are dependent on the concentrations within each department, this model is described by a system of first-order differential equations:

$$\frac{dC_{ND}(t)}{dt} = K_1 C_P(t) - (K_2 + K_3) C_{ND}(t) + K_4 C_S(t)$$

$$\frac{dC_S(t)}{dt} = K_3 C_{ND}(t) - K_4 C_S(t)$$

(4)

This system can be solved completely through non-linear estimation using maximum-likelihood algorithms, though it is computationally expensive work. When the entire system is solved, and rate constants are estimated, the V_T is found to be:

$$V_T = \frac{K_1}{K_2}\left(1 + \frac{K_3}{K_4}\right)$$

(5)

A disadvantage of CM is that radiotracers must be fully characterized and understood by investigators in order to choose a parsimonious compartment model that produces the most accurate and reproducible result. It is sometimes not obvious what compartment configuration is appropriate for a given radioligand-receptor complex study, and testing of multiple compartmental models must be carried out. The other two methods discussed in this section do not require prior selection of compartment configuration.

Systems developed in dynamic PET by CM are usually linear and time-invariant (LTI). A linear system will obey the principle of superposition[47]. Putting two signals through the system and adding the results would be the same as adding the two signals and then passing the sum through the system. For a time-invariant system, adding a delay to the input signal would simply

result in the output signal acquiring the same delay. As such, the output can be defined as the convolution between the input function (typically C_P) and the impulse function (IR):

$$C_{PET}(t) = C_P(t) \otimes IR(t)$$

$$C_{PET}(t) = \int_{-\infty}^{\infty} C_P(\tau) \, IR(t - \tau) d\tau$$

(6)

An alternative to CM is spectral analysis (SA). SA is a technique commonly used in fields that perform a lot of signal processing, like Astronomy and Electrical Engineering. It is based on the idea that the LTI time series can be represented by an analytically summed series of exponentials, each with its own frequencies[48,49]. Using the CM description from equation 4, we define the IR to be a series of summed exponentials:

$$C_{PET}(t) = \sum_{i=0}^{N} C_P(t) \otimes \alpha_i \cdot e^{-\beta_i t} = \sum_{i=0}^{N} \alpha_i \, \beta_i(t)$$

(7)

N is the number of tissue responses being summed in order to model the tissue uptake and is chosen to be a large number (typically around 1000) to allow for high granularity. Values of β_i are predetermined and designed to cover a spectral range that will account for both slow transfer responses and transient phenomena like the passage of the radiotracer through the vasculature in the area. Values of α_i are solved by a non-negative least-squares procedure using the PET tissue activity and the input function. As SA modeling is based upon a compartmental system described by first-order differential equations, parameters and coefficients are restricted to be real and non-negative[50]. In PET systems, only a few values of α_i will be non-negative, leading to a kinetic spectrum of peaks like those seen in Figure 6. An advantage of SA over CM is that there is no imposed specific compartment structure, and if fact, the results of SA can indicate the number of compartments appropriate for the system based on the number of spectral peaks resolved.
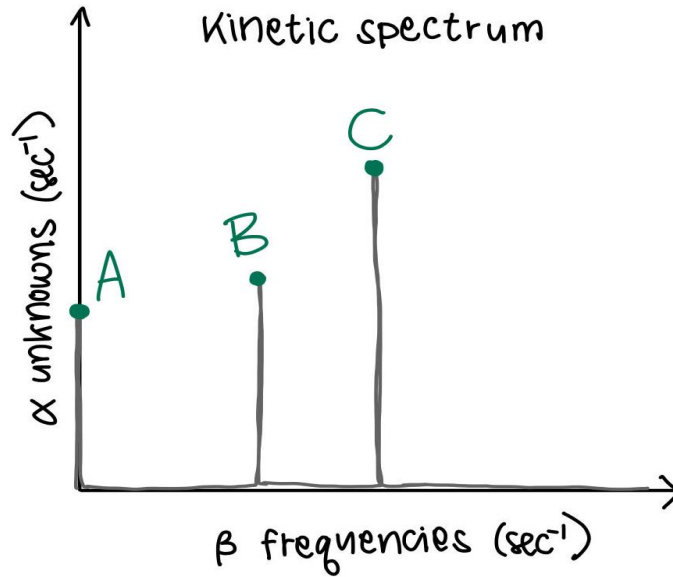
Figure 6: A simplified pictorial example of a kinetic spectrum that might result from spectral analysis of a pharmacological system. The peak at A indicates that there is an irreversibly binding (during the time span of the scan at least) component. Peak B and C indicate that there are two reversibly binding components that will have transfer into and out of them.

The number of peaks (β with $\alpha > 0$) corresponds to the number of distinct compartments. A peak to the far left ($\beta \cong 0$) is due to a low-frequency component that indicates irreversible tissue binding. A peak to the far right ($\beta \rightarrow \infty$) is due to a high-frequency component that indicates vascular contributions. Peaks in between these two extremes can be attributed to reversible binding between compartments[51]. The V_T can then be estimated from spectral analysis by the following relationship:

$$V_T = \sum_{i=1}^{N} \frac{\alpha_i}{\beta_i} \tag{8}$$

SA does not allow for the exact solutions of macroparameters of interest or even estimation of transfer rate coefficients, making it a less rigorous solution than CM. However, it does allow us to separate transient vascular effects in a way that CM does not, which can be a major advantage in some situations. SA is not used regularly in the field but is accumulating growing support.

Another alternative to CM is the implementation of graphical analysis (GA) for kinetic

quantification. The main idea behind the graphical approach for quantification is to transform the

data into new variables that are linearly related so that parameters of interest can be solved by

simple systems of linear regression[52]. Most commonly used in PET studies is the method

introduced by Logan et al.[53], dubbed the Logan Plot. The Logan plot method is designed to be

used for ligands that bind reversibly in tissue and whose complexes can be accurately described

by a one or two tissue CM.
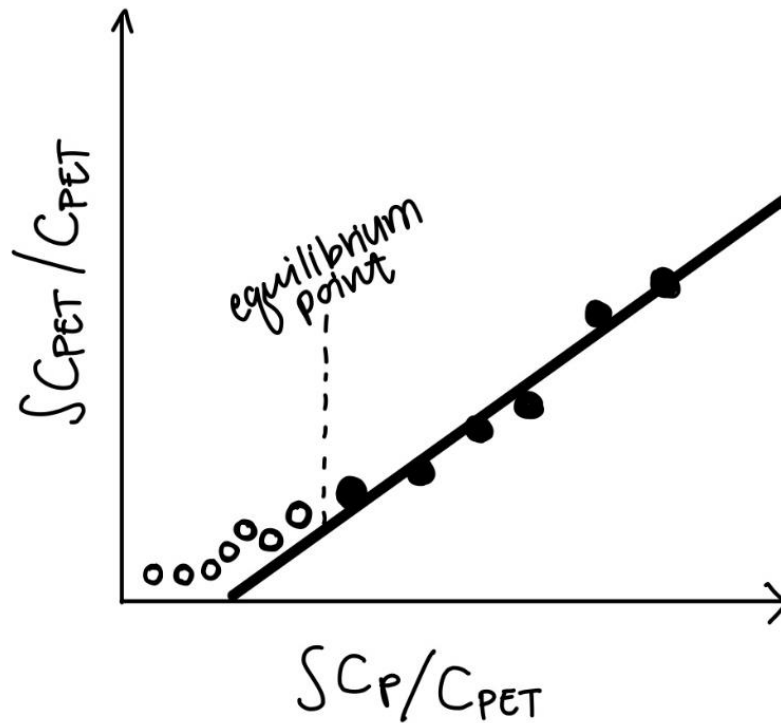
Figure 7: A simplified pictorial example of Logan plot that might be created with PET data. This graphical analysis method transforms the compartmental relationships into a linear system that can be solved by using simple regression once equilibrium has been reached.

Again, the theory behind the Logan GA method stems from the system description

established by CM. Differential equations given in equation 4 are transformed in such a way as

to leave us with the linear relationship:

$$\frac{\int_0^t C_{PET}(\tau)d\tau}{C_{PET}(t)} = V_T \frac{\int_0^t C_P(\tau)d\tau}{C_{PET}(t)} + b \qquad (9)$$

Equation 9 allows for V_T to be solved through simple linear regression, where b is the y-intercept, and V_T is the slope[54]. In this derivation, it is assumed that the signal contribution from blood in vessels is small enough to be negligible. Benefits of using the Logan GA are its simple methodology, fast computation time, and independence from a strict kinetic model. A non-linear estimation algorithm, like what is necessary for SA, is highly dependent on initial parameter guesses. Importantly, the same is *not* true for the linear optimization methods employed with GA. A requirement of the Logan GA method is that the system must have reached equilibrium before analysis can occur and parameters solved. The limitations of the Logan GA method include this equilibrium timing constraint and its inability to fully describe the physiology of interest. Logan plots are routinely used in the field, with many [^{11}C]PBR28 studies[55-57] exclusively using this method for quantification due to its computationally simple algorithms.

As no previous studies have yet evaluate PBIF performance with more than one quantification method, it is possible that other methods noted above would show less sensitivity to changes in the IF and thus perform better than previously published methods. Therefore, this thesis will test PBIF performance with these three quantification methods to evaluate the most comparable V_T between the arterial IF modeling and the PBIF modeling.

2.6 Clinical relevance in Methamphetamine-use Disorder.

Chronic drug addiction is a national and global public health concern[58]. SUDs present with a host of deleterious side effects that harm the user and society at large. Of particular concern in the Northwestern US is MA. MA is a drug that affects the dopamine (DA) and norepinephrine receptors of the CNS to elicit feelings of alertness, euphoria, and well-being.

Negative symptoms include increased blood pressure, cardiac arrhythmia, stroke, shaking, increased anxiety, insomnia, aggressive tendencies, paranoia, and hallucinations[59]. According to the 2020 National Survey on Drug Use and Health, about 1.5 million people in the US have a MUD.

MA is a derivative of amphetamine which was utilized medicinally as early as 1932 and became mass marketed during the first world war when it was given to soldiers and factory personnel to stave off tiredness and increase endurance. The first epidemic of MA abuse took place shortly after the war, following army surplus being released to mass civilian markets. Recreational MA is often injected intravenously or smoked but can also be snorted or ingested.

Users of MA often struggle to maintain abstinence as discontinuing drug use is usually accompanied by depression, fatigue, cognitive impairment, and intense cravings. Compared to other substance use disorders, rates of inpatient hospitalization for MUD are high due to the high rates of medical complications and side effects. As there are no FDA medications for MUD, the use of MA is widespread, particularly in low-income populations who often have limited access to medical interventions and treatment.

A large body of evidence suggests that deficits in decision-making and self-control associated with MUD are moderated by abnormalities in the DA system from chronic MA exposure. Long-term effects include a decrease in DA D2 receptor binding, deficits in functional activation and connectivity in dopaminergic brain regions, and abnormalities in regional brain volumes and structural white matter integrity[4]. Animal studies show that DA production was significantly reduced after just ten days of MA use and took two years to fully recover in a study using [18F]fluoro-L-DOPA PET[2]. In addition to actions of MA on monoamine signaling pathways contributing to functional brain and cognitive deficits, excess DA and glutamate

neurotransmission with chronic MA exposure induces neurotoxicity and increases inflammatory cytokine production and expression of factors associated with activated microglia. Chronic cytokine exposure decreases striatal DA release and striatal D2 type receptor availability in cytokine-treated non-human primates. This decrease in DA release is associated with reductions in sensitivity to rewards. As studies provide evidence that neuroinflammation and MA use affect multiple aspects of DA function that may interact to promote functional brain abnormalities present in addiction, investigating the link between neuroinflammation and brain function in MUD may provide biomarkers for treatment targets and interventions.

METHODS

3.1 Subjects

This IBR approved study recruited volunteers diagnosed with MUD(DSM-IV) from the Veterans Affairs Portland Healthcare System (VAPORHCS) and community substance abuse treatment programs. Healthy controls we recruited via online advertisements. All volunteers were provided written informed consent, as approved by the VAPORHCS and Oregon Health & Science University Institutional Review Boards. Exclusion criteria, determined by medical history and laboratory blood tests were: systemic, neurological, cardiovascular, or pulmonary disease, head trauma with loss of consciousness, magnetic resonance imaging (MRI) contraindications, use of medications known to have dopaminergic mechanisms (e.g., antipsychotics, antidepressants, antiparkinsonian agents), sedative-hypnotics (e.g. barbiturates, benzodiazepines, zolpidem) or anticholinergics. Past or Current Axis I diagnoses, other than MA dependence (MA group) or nicotine dependence (either group), assessed with the Structured Clinical Inventory for DSM-V, were exclusionary. Urine testing on the day of the MRI scan verified abstinence from cocaine, methamphetamine, benzodiazepines, opiates, and cannabinoids. Participants were allowed to smoke cigarettes up to one hour before scanning to minimize and balance the effects of recent smoking on brain function against the effects of nicotine withdrawal and craving.

3.2 PET Imaging

PET imaging was performed on the Philips® Vereos Time-of-Flight Scanner at the VAPORHCS. This system is reported by the vendor to have a maximum spatial resolution of 4.1 mm and a timing resolution of 310 kilo-counts per second. [^{11}C]PBR28 was prepared at the Center for Radiochemistry (CRR) cyclotron facilities at Oregon Health & Science University

under an FDA Investigational New Drug (IND) protocol. Once manufactured, the radiotracer dose undergoes quality control at the CRR to ensure acceptable purity. After arriving at the VAPORHCS nuclear medicine department from the CRR, it undergoes one last round of quality assurance to make sure the activity is within tolerance limits of the prescribed dose of 0.2 mCi/kg with less than 5 µL of PBR28 per mL of injectate. With the assistance of the nuclear medicine technologists, subjects are positioned on the scan bed with their brains centered axially within the FOV. The patient first undergoes a CT scan for attenuation correction. If the dose has passed all QC and the activity is within the correct range, it is injected through an intravenous (IV) catheter, and the PET detectors begin acquisition. The dynamic series includes 25 image frames with lengths ranging from 15 seconds to 10 minutes. The entire duration of the scan is 90 minutes.

3.3 Venous or Arterial Sampling Procedure

HC subjects had a radial arterial line placed in one arm for blood sampling and an IV line in the other for tracer injection. In the case of an arterial line failure or if there is no medical staff available to facilitate the line set-up, both arms receive IV lines, one for injection and one for blood draws in opposite arms to avoid cross-contamination that would affect the blood activity counts. In MA subjects, we only set IV lines were placed due to their compromised vasculature and their concomitant risk comorbidities.

During PET scan acquisition, 19 serial blood samples were manually drawn from the arterial or non-injection IV line at specific time points and processed within the PET suite by the study research staff. Specifically, blood draws were obtained in the following time course: one milliliter was obtained every 30 seconds for the first 4 minutes, every minute for 6 to 10 minutes after injection, every 5 minutes from 20 to 30 minutes after injection, and every 10 minutes from

40 to 90 minutes after injection. Samples were immediately microfuged and their activity was measured using a Ludlum^{TM} gamma spectrometer.

Blood volumes used for measurement and the counting time lengths were standardized in order to aid ease of processing and to reduce the risk of error due to human error. The first half of the samples are counted for one minute using 200 µl of whole blood or plasma. Halfway through the scan, the volumes and counting times are doubled to maintain statistical strength as the decaying activity results in waning count rates. Using three samples spread throughout the length of the scan, we measure the activity in the whole blood. Some of the radiotracer and radiometabolites will become attached to red blood cells and contribute to image signal without being available in the plasma compartment to pass into brain tissue and bind to receptors. Modeling software, Pmod^{TM}, requires both plasma activity and whole blood activity to account for the signal coming from the whole blood.

Small amounts of each of the 19 blood samples were spun down in a centrifuge to separate the serum from the red blood cells. For all 19 samples, the specified volume of plasma was pipetted into a counting tube and put into the bore of the well counter for measurement. Not all of the radioactive material that is in the plasma is available for receptor binding. When a pharmaceutical is injected into the bloodstream, it will end up in a variety of states because of the complex chemical environment of the circulatory system. Some of the radiotracer pharmaceutical will be broken down into one or more derivative compounds known as metabolites[60]. At least one of these metabolites will contain the radioactive isotope but will not behave in the same way as the intended parent radiotracer. Accounting for this radiometabolite contribution to the image signal will be described in the data analysis section (3.4.1).

3.4 Data Analysis

3.4.1 Corrections and Calibrations

The PET scanner will apply multiple corrections and calibrations, and the final data will be in units of activity, typically kilobecquerels (kBq). In order to perform kinetic modeling, blood data also need to be in units of activity. Raw blood activity measurements are in the number of counts detected per unit of time, typically counts per minute (cpm). To convert cpm to kBq, we need to calculate a calibration factor that will account for counter sensitivity and efficiency. We performed the calibration experiment with the gamma counter in the exact location it is in during scans using a pure dose of [^{11}C]PBR28. Knowing the precise activity of the dose at a specified time, the inherent sensitivity and efficiency of the counter were measured and a calibration factor was calculated that would later be applied to blood data to convert from cpm to kBq.

Background radiation is always present and contributes to the count signal even through the lead shielding of the well counter. Celestial and terrestrial sources of background do have a small contribution to the signal, but the main contributions are from the injected subject and from the blood samples collected near the processing bench, which are both inherently radioactive. In an effort to account for these sources of radiation, dark counts are taken throughout the scan. These background counts are fit to a decaying exponential curve which is used to correct each blood draw by subtracting the estimated background counts per minute from the collected counts per minute at each time point.

3.4.2 Metabolite Processing

The radiometabolites are usually less lipophilic than the original tracer and so are less likely to cross over the BBB and into the brain tissue. When constructing the plasma IFs, it is

vital to ensure only the unmetabolized parent radiotracer concentration in plasma is used as that is what needs to be reflected in the plasma modeling compartment. Using ion exchange filters and solid phase extraction techniques, metabolites are separated from the plasma based on their polarity and chemical characteristics. By measuring the activity left in these columns and the activity in the plasma which has been pushed through, the fraction of unchanged parent radiotracer within the plasma, known as the plasma parent fraction (PPf), can be determined. The HPLC process is time-consuming and resource-expensive, and so is only performed for 8 of the 19 samples. The PPf as a function of time is constructed by fitting through least squares regression to a modified hill model given by Tonietto et al.[60] that is specific for [^{11}C]PBR28:

$$PPf(t) = \frac{\left(1 - \frac{t^3}{t^3 + 10^a}\right)^b}{1 + c} \quad (10)$$

$$C_P(t) = C_{tot}(t) \cdot PPf(t)$$
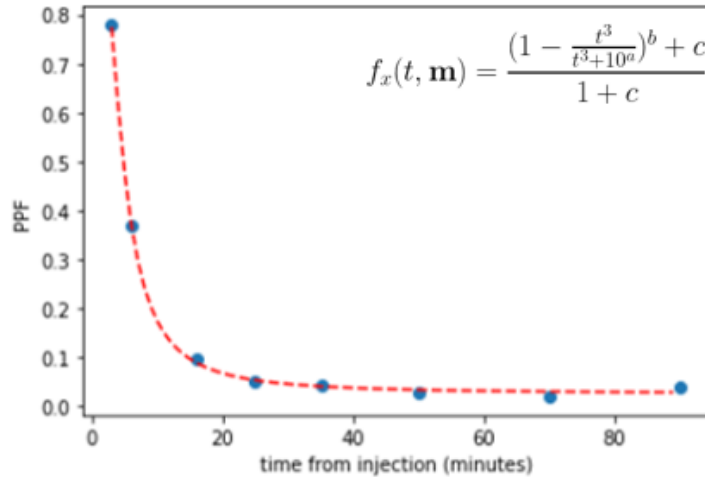
Figure 8: Processed metabolite data are plotted and fit to a modified hill function to construct the parent plasma fraction (PPF). The PPF will be used to correct all plasma values to only reflect the unchanged radiotracer.

3.4.3 Derivation of Population-Based Input Function

The calibrated blood activity data are decay corrected to the time of injection. In this way, it is ensured that the variation in activities across time points is due to biological processes,

not the physical decay of the radioisotope. The PET scanner software will automatically do the

same for scan signal data. Plasma input functions for every subject were constructed by fitting a

decaying tri-exponential function (equation 12) suggested by Pmod[TM] documentation[51] to the

fully corrected unmetabolized plasma activity data through least-squares estimation using the

SciPy package in Python. Although Pmod[TM] provide a package to perform this fit, Python

implementation allows flexible customization of starting parameters and is more computationally

efficient.

$$C_P(t) = \begin{cases} linear\ interpolation\ ;\ t < begin \\ \sum_{i=1}^{3} A_i e^{(t-begin)ln2/B_i}\ ;\ t \geq begin \end{cases} \qquad (\,11\,)$$

For the generation of PBIFs, a leave-one-out method was implemented in order to not

introduce bias and overfitting into the results. The number of subjects will correspond to the

number of PBIFs generated for testing. The first step was to construct data sets of time activity

information from the derived arterial IFs. With N subjects, plasma time activity data from N-1

IFs were loaded into a concatenated data frame and fit to the same decaying exponential function

given in equation 12. The resultant PBIF was assigned to the subject whose data was left out

during its construction.

Second generation TSPO ligands have notoriously high intersubject variability. This

simple averaging method for PBIF generation will likely need to be augmented by scaling of the

PBIF based upon some metric specific to the subject. Previous studies have done this with one or

a few arterial or venous blood activity levels from samples drawn at optimized times[61]. This

method still requires invasive sampling but modestly alleviates patient burden by reducing the

number of required blood draws. This scaling method was tested by scaling by blood activity at a

single time point across all subjects. In order to determine the most optimal time point, the area

under the curve (AUC) from the PBIFs scaled by activity at each time point was compared to the
AUC from the arterial IFs to obtain the residual sum of squares (RSS). After analysis of all the
available time points, the time point with the lowest RSS was used for scaling. The limitation of
this blood activity scaling method is that for this study, the PBIF generated with data from HCs
with only arterial sampling data is applied to the patient group with only venous sampling. It is
unclear whether validation of arterial blood activity scaling translates to the venous blood
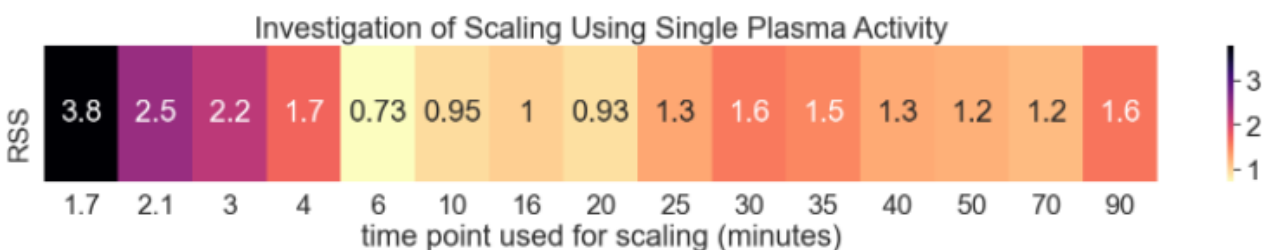activity scaling in the patient group.

*Figure 9: Residual sum of squares (RSS) of the ratio IF AUC to PBIF AUC using blood activity scaling at different
time points when compared to a ratio equal to 1 (PBIF AUC = IF AUC). Based on these values, I chose to scale by
the blood activity at six minutes as this had the lowest RSS.*

As these limitation warrant caution, alternative scaling methods were tested. Scaling by
injected activity, injected activity divided by patient size, and subjects' genetic binding affinity
classification all resulted in worse performance than the non-scaled PBIF. As PBR28 exhibits
high lipophilicity in order to cross the BBB[62], scaling by body mass index (BMI) was
investigated. The lipid solubility of $[^{11}C]$PBR28 enables peripheral adipose tissue uptake which
reduces the concentration in the plasma available to cross the BBB and bind with the TSPO
receptors. Because of this, I hypothesize that differences in the range of body fat could be
contributing to intersubject variability, making it a promising metric by which to scale. BMI is
calculated as an individual's weight in kilograms divided by the square of their height in meters.
As such, it is not a true measure of body fat since it doesn't take into account natural variation in
the ratio of lean and adipose tissues and other bodily constituents. However, it is employed

clinically and in many research fields as an estimate of body fat levels because of its general correlation and wide history of use.

Each subject's BMI was plotted against the arterial IF AUC to PBIF AUC ratio which was fit to a decaying exponential (equation 12) where parameters a and b were optimized. The RSS using the unscaled PBIF was 24.6. After BMI scaling, the RSS was 3.92. This is a larger RSS than those seen from the blood activity scaling investigation (figure 9) but is still a dramatic improvement from no scaling.

$$\text{Scaled PBIF} = \text{PBIF} \times Y$$
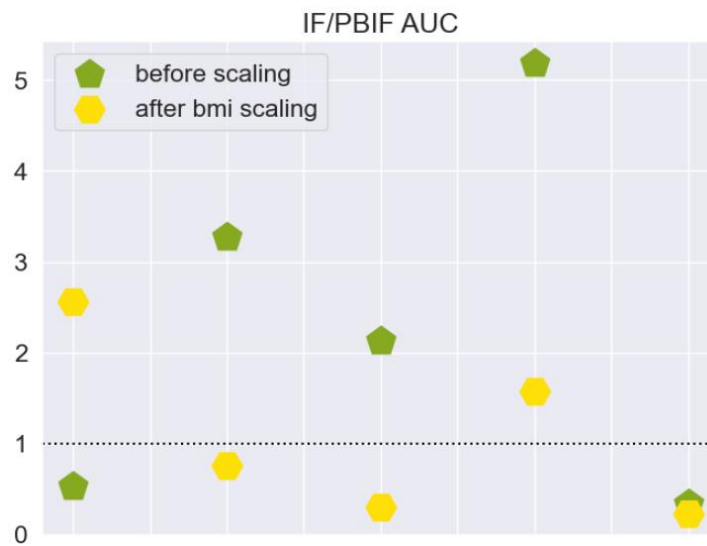
$$Y = ae^{-b \times BMI}$$

(12)

Figure 10: Testing of the BMI scaling method established for this study. Each vertical line is the ratio of IF AUC to PBIF AUC for a HC subject. In an ideal world, this ratio would be 1 for all points. The green pentagons show the ratio with the raw PBIF with no scaling. The yellow hexagons show the rations with the PBIF have applying BMI scaling. The residual sum of squares improved from 24.6 to 3.92.

For both the blood activity and BMI methods, the scale factor was based on the AUC of the plasma IFs. To investigate which scaling method resulted in stronger correlations to the gold standard arterial IFs, PBIFs scaled by both methods and the PBIF with no scaling were included in kinetic modeling to get V_T.

3.4.4 Dynamic PET Processing

The dynamic PET data were processed using PNEURO[63] , a tool provided by Pmod[TM]. The first step in the analysis pipeline is to import the DICOM files from the scans and inspect them to ensure image quality is acceptable and there are no significant artifacts or other issues. One of the study PET scans had corrupted frame slicing that was flagged at this step. The corruption created doubt about the accuracy of kinetic modeling with this data and so was excluded from V_T calculations for the purpose of this thesis.

The next step is to load the corresponding T1-weighted MR image for anatomical registration. MR images were previously processed for cropping and defacing, but this processing can be performed in PNEURO if needed. The software will segment the gray matter, white matter, and cerebrospinal fluid using probability maps. Next, the averaged PET image is rigidly matched with the MR image. Rigid matching is sufficient if MR and PET images are acquired in sufficiently close succession for brain imaging. Visual inspection was performed and any minor adjustments were made accordingly.

MRI data from subjects' brains were then transformed into a standard anatomical coordinate space through normalization. The default atlas, N30R83, in the head-first supine orientation was used as this is the most commonly applicable space. This atlas is based upon the description of the brain and its structures detailed by Hammers et al.[64] and consists of 83 distinct brain regions contoured onto the MRIs of 30 healthy subjects. Normalization results in a mapping of the MR to the standard atlas. This MR-atlas mapping and the previous PET-MR matching allow the software to bootstrap a mapping of the PET to the atlas space. The different brain regions are outlined in all three spaces based on this mapping. The four ROIs chosen for

this analysis include the whole brain, the cerebellum, the ventral striatum (including the caudate nucleus, the nucleus accumbens, and the putamen), and the amygdala/ hippocampus.

3.4.5 Kinetic Modeling

TACs for each chosen ROI were be calculated and exported along with Ifs to the Pmod^{TM} kinetic modeling tool, PKIN[51] to perform kinetic modeling . The software has a library of modeling methods that can be applied to data to generate optimized model-specific parameters. For CM, these are the scaling amplitude and transfer rates for each compartment. For SA, we are optimizing the α's and β's. And for Logan GA, these parameters are the start time corresponding to when equilibrium is reached and the slope and intercept of the linear regression. It is important to cycle through guesses of these starting parameters when using CM or SA in order to ensure you are obtaining the best fit, as initial values will have significant effects when using iterative estimation methods. Once the model parameters were optimized, the corresponding V_T from each method, for each participant, in each brain region was generated using arterial IFs and then using the PBIFs. As kinetic modeling is highly dependent on ROI contouring, IF and PBIF analyses were performed using the same ROI definitions and tissue TACs.

3.5 Statistics

3.5.1 Comparison of Plasma Activity Between Groups

The first aim of this thesis is to make sure that the plasma activity concentrations between the MA group and the HC group are not statistically different. Common statistical tests like the two-sided t-test and analysis of variance (ANOVA) are insufficient for this purpose because while a low p-value would lead to the conclusion that there is a statistically significant difference between the two groups, a high p-value does not allow us to draw conclusions in the opposite

direction to say that there is not a difference between the groups. It is erroneous to use statistical

tests in this way to confirm agreement. Therefore, we implement equivalency testing, which was

actually developed in the field of pharmacokinetics in the 1980s[65]. Equivalency testing provides

support for the absence of any meaningful effects by setting equivalence bounds based on

standardized effect sizes defined and justified by the investigator. Effects small enough to be

deemed insignificant by this defined criterion can be rejected. When we reject an effect, we can

act as if the true effect is close enough to zero for practical purposes.

The decision to use equivalency testing for these analyses provides the flexibility to

define boundaries that are clinically significant. As arterial sampling method is the gold standard

and this data is used to generate and test PBIFs within this group, equivalency bounds will be set

based on the normalized intersubject variability seen in this group. We will need to normalize the

AUCs by dividing each AUC value by the average AUC value for the group we're comparing. If

the AUCs are all close to each other, this will result in values close to one. Big differences in

AUCs will mean these values will be further from one. The standard deviation seen in the HC

arterial group was calculated and the equivalency bounds we set to be one plus or minus 1.96

times this standard deviation.

3.5.2 Comparison of V_T: Arterial IF Versus PBIF

The second aim of this thesis is a methodological comparison to determine whether use

of a PBIF provides results consistent with the results from the currently accepted or gold-

standard method of using an arterial IF. As with any research aim, we need to establish our

statistical analysis framework before analyzing data and drawing conclusions. The commonly

employed t-test and ANOVA are inappropriate for agreement studies because they only measure

the difference between the means of two groups, while we are interested in directly comparing

the individual results of each subject using two different methods. To feel confident using a PBIF as an alternative to arterial sampling, the results from both methods must be strongly correlated to indicate high precision and also within statistical agreement to indicate high accuracy.

The first step is to examine the correlation between two methods. If the two methods were exactly the same, they would fall along the diagonal line $y = x$. In practice, they will have some spread about a line with an arbitrary slope. Parametric linear regression is performed and SciPy tools are used to extract the Pearson correlation coefficient (r-value), which is a measure of the linear correlation between two variables. I will consider a strong correlation to be r > 0.75 based on literature trends in similar fields.

If a high correlation exists, the next step will be to ensure agreement within statistical constraints. A formal implementation of agreement analysis was developed by Bland and Altman in the 1980s for methodological comparison studies[66]. The analysis involves plotting the difference between the two methods against the average to obtain 95% confidence intervals for clinical consideration. Krouwer[67] suggests that when one of the methods is considered a gold standard, the difference between methods should be plotted against the gold standard, not the average. Because arterial sampling is the accepted gold standard in kinetic modeling, I will be using the Krouwer modification of the Bland-Altman statistical method to compare results from PBIF and arterial IF for agreement.

RESULTS

4.1 Input Functions

After correcting and calibrating blood data from the HC and MA subjects, plasma activity curves were constructed for each individual using the SciPy package in Python. Each set of data was fit to equation 12 using least squares regression. Two HC subjects had to be excluded from the analysis due to errors with blood data collection resulting in data being too messy to correct and fit. This analysis includes 5 HCs with arterial sampling, 4 HCs with venous sampling, and 8 MA users with venous sampling. The plots below represent the blood activity data, either from venous or arterial sampling, and the IF that was fit to those data. For the HC subjects who did have arterial sampling, the PBIF that was generated without data from the specific subject is plotted next to their plasma activity data and arterial IF for comparison. This PBIF is what was used for modeling to obtain the values of V_T reported later.

Visual inspection of the PBIFs reveals a clear variability in how well the PBIFs match the arterial IFs between subjects. The match between the two IFs is worse toward the beginning of the scan before equilibrium has been reached. Subjects 209 and 968 had noticeably lower activity levels overall in their plasma samples as revealed by the AUCs in table 1. The PBIFs for these subjects are visually more different from the arterial IFs as seen in figure 11.
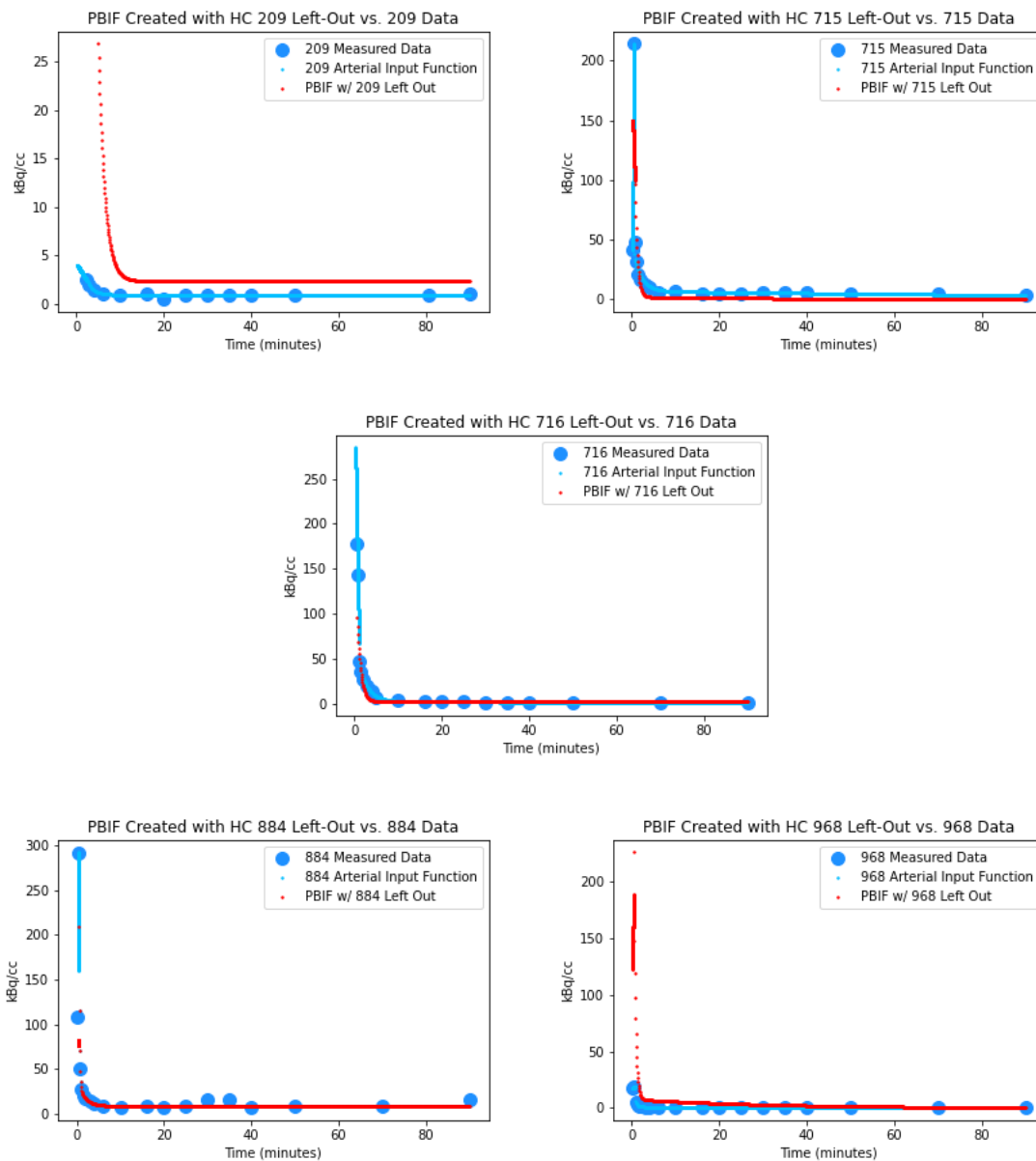
Figure 11: Time activity plots, fitted arterial IFs, and generated PBIFs for all of the HC subjects who underwent arterial sampling.
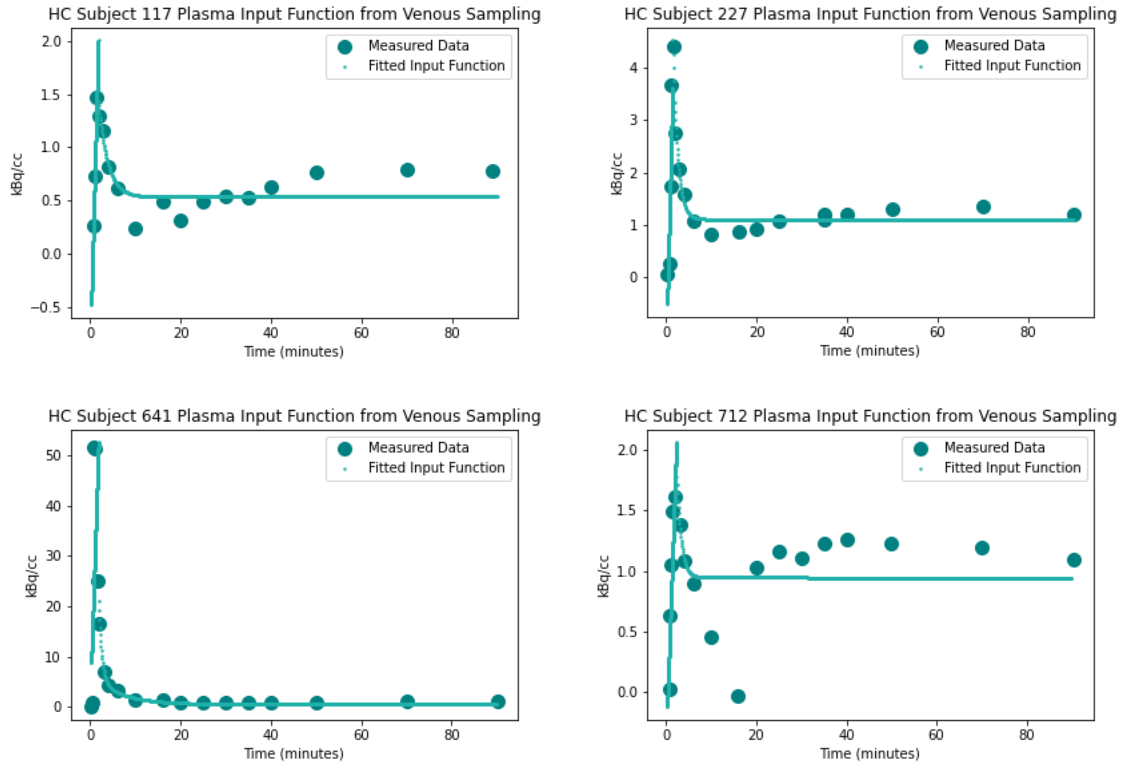
Figure 12: Time activity plots and arterial IFs for all of the HC subjects who underwent venous sampling.
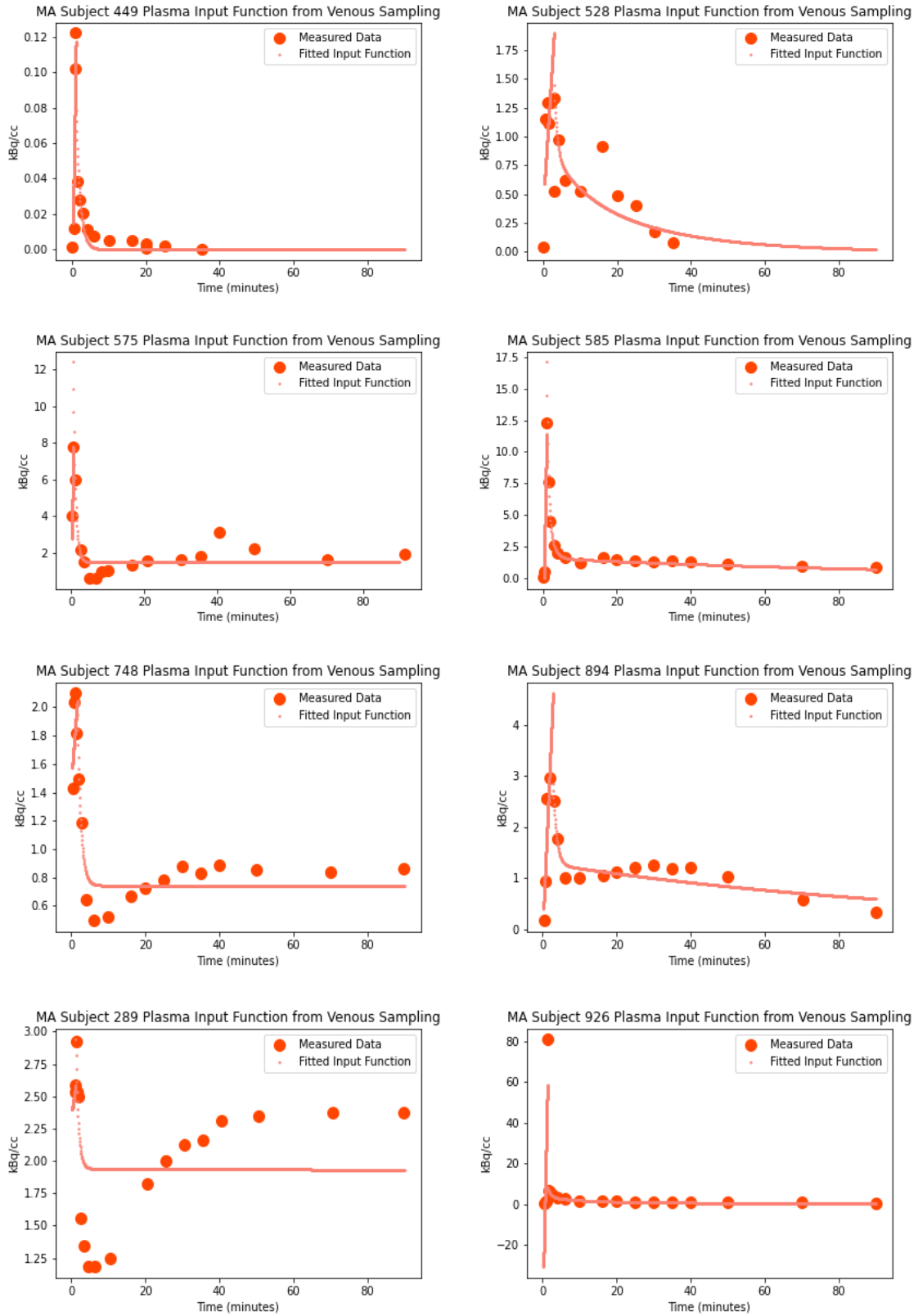
Figure 13: Time activity plots and arterial IFs for the MA subjects, all of whom underwent venous sampling

The AUC, a measurement of total activity during the time course of the scan, was calculated through definite integration from 0.25 minutes to 90 minutes post-injection. Integration was performed in Python using the integrand function from the SciPy package.

Table 1: Total plasma activity during the course of the PET scan for all subjects

Subject	IF AUC (kBq)	Subject	PBIF AUC (kBq)	Subject	IF AUC (kBq)	Subject	IF AUC (kBq)
HC w/ Arterial Plasma Samples		HC w/ Arterial Plasma Samples		HC w/ Venous Plasma Samples		MA w/ Venous Plasma Samples	
209	112.19	209	456.47	117	66.19	289	233.26
715	705.02	715	159.16	227	136.43	449	0.14
716	457.30	716	322.97	641	157.81	528	21.81
884	1116.60	884	226.83	712	114.19	575	186.43
968	72.89	968	443.91			585	144.42
						748	91.58
						894	105.51
						926	95.20

Table 1 lists the AUC of each subjects' plasma IF, based on venous or arterial sampling measurements. HCs with arterial sampling also have an AUC of their PBIF listed. This is the PBIF assigned to them for modeling that was generated with their data left out. These data show the high levels of inter-subject variability. The arterial sampling HC group showed the largest variability with a standard deviation of 435 kBq. Data from venous sampling in the HC and MA groups resulted in standard deviations of 39 kBq and 78 kBq, respectively.

4.2 Volume of Distribution

Kinetic modeling was performed through the PNEURO and PKIN packages provided by Pmod[TM] on the PET data from HCs with arterial sampling. V_T is reported in units of ml/cm^3. One of the HCs who had arterial sampling data had a PET scan file that was corrupted and could not

be fixed in time for the analysis of this thesis. The below tables list the V_T values for all brain regions in all subjects, using all modeling and scaling methods.

Table 2: V_T in all brains regions of all subjects using the 2-tissue-compartmental modeling technique

2-Tissue Compartmental Model	V_T from IF	V_T from PBIF		
		No Scaling	Blood Scaling	BMI Scaling
Subject 209				
Whole Brain	8.911	1.642	2.053	10.736
Cerebellum	8.937	1.674	2.102	11.179
Ventral Striatum	7.162	1.361	1.716	8.978
Amygdala-Hippocampus	10.269	1.913	2.397	12.552
Subject 715				
Whole Brain	1.543	3.194	2.416	1.835
Cerebellum	1.968	4.000	3.009	2.294
Ventral Striatum	1.624	3.317	2.511	1.906
Amygdala-Hippocampus	1.584	3.381	2.696	2.058
Subject 716				
Whole Brain	0.829	2.624	0.374	1.571
Cerebellum	1.019	3.191	0.454	1.910
Ventral Striatum	0.730	2.284	0.328	1.370
Amygdala-Hippocampus	0.828	2.663	0.380	1.600
Subject 884				
Whole Brain	1.068	3.810	1.665	2.630
Cerebellum	1.349	4.704	1.940	3.053
Ventral Striatum	1.088	3.855	1.518	2.411
Amygdala-Hippocampus	1.091	3.903	2.082	3.226

Table 3 lists the V_T obtained through CM in the arterially sample HCs using all IFs. Without scaling the PBIF, there was an average percent difference of 165 ± 74 between the arterial IF and PBIF results. When we scaled the PBIF based upon blood activity at a single time point, there was a 62 ± 14 average percent difference. And scaling the PBIF based upon subject

BMI resulted in an average percent difference of 70±57. The V_T was significantly higher in

subject 209 for unknown reasons, but the results from the BMI scaled PBIF matched these high

values.

Table 3: V_T in all brain regions using the spectral analysis technique. Note that spectral analysis failed for one set of patient data using Pmod^{TM} and a separate spectral analysis specific software, SAKE, even after consultation with the creator of the software

Spectral Analysis	V_T from IF	V_T from PBIF		
		No Scaling	Blood Scaling	BMI Scaling
Subject 209				
Whole Brain				
Cerebellum				
Ventral Striatum				
Amygdala-Hippocampus				
Subject 715				
Whole Brain	1.331	3.117	3.284	2.512
Cerebellum	1.641	3.916	4.302	3.297
Ventral Striatum	1.435	3.261	2.901	2.214
Amygdala-Hippocampus	1.436	3.369	3.705	2.839
Subject 716				
Whole Brain	0.725	2.596	0.371	1.559
Cerebellum	0.970	3.152	0.450	1.893
Ventral Striatum	0.676	2.269	0.324	1.363
Amygdala-Hippocampus	0.805	2.640	0.377	1.585
Subject 884				
Whole Brain	1.013	3.797	1.568	2.483
Cerebellum	1.217	4.678	1.827	2.893
Ventral Striatum	0.986	3.834	1.432	2.268
Amygdala-Hippocampus	1.082	3.876	1.960	3.104

Table 4 lists the V_T obtained through SA in the arterially sample HCs using all IFs. These

values are similar to those obtained via CM, with an average difference 9% between the two

quantification techniques when using arterial IFs. Without scaling the PBIF, there was an average percent difference of 216±64 between the arterial IF and PBIF results. When we scaled the PBIF based upon blood activity at a single time point, there was an 84±46 average percent difference. And scaling the PBIF based upon subject BMI resulted in an average percent difference of 112±34.

Table 4: VT in all brain regions from all subjects using the Logan graphical analysis technique

Logan Graphical Analysis	VT from IF	VT from PBIF		
		No Scaling	Blood Scaling	BMI Scaling
Subject 209				
Whole Brain	6.534	1.247	1.588	8.308
Cerebellum	6.727	1.288	1.643	8.592
Ventral Striatum	5.480	1.061	1.357	7.097
Amygdala-Hippocampus	7.675	1.465	1.868	9.774
Subject 715				
Whole Brain	1.428	2.954	2.082	0.568
Cerebellum	1.782	3.620	2.420	0.604
Ventral Striatum	1.522	3.135	2.230	0.497
Amygdala-Hippocampus	1.497	3.176	2.419	0.570
Subject 716				
Whole Brain	0.765	2.305	0.329	0.051
Cerebellum	0.928	2.788	0.398	0.053
Ventral Striatum	0.667	1.978	0.282	0.058
Amygdala-Hippocampus	0.786	2.362	0.337	0.049
Subject 884				
Whole Brain	0.945	3.612	1.173	0.427
Cerebellum	1.154	4.409	1.374	0.404
Ventral Striatum	0.935	3.599	1.105	0.387
Amygdala-Hippocampus	0.987	3.732	1.320	0.508

Table 5 lists the V_T obtained through Logan GA in the arterially sample HCs using all IFs. These values are also similar to those obtained via CM, with a slightly higher average difference of 13% between the two quantification techniques then SA. Without scaling the PBIF, there was an average percent difference of 167±82 between the arterial IF and PBIF results. When we scaled the PBIF based upon blood activity at a single time point, there was a 51±20 average percent difference. And scaling the PBIF based upon subject BMI resulted in an average percent difference of 60±24.

With all quantification methods, the non-scaled PBIF produce V_Ts that were the most different from the V_T produced using arterial IFs. The differences seen from the blood activity and BMI scaling methods were within one standard deviation of each other with all quantification methods. There appears to be no trend between brain ROI and performance, so the data will be concatenated together for analysis. The significance of these data and their interpretation are presented in the discussion section.

DISCUSSION

5.1 Comparison of Plasma Activity Between Groups

The first step was to set the equivalency bounds which will define statistical significance as outlined in the Methods section (3.5.1) using AUCs from the arterial IFs of HCs (Table 1). It was found that the standard deviation of the normalized AUCs in the HCs was 0.789, resulting in equivalency bounds of [-0.547,2.547] based upon 95% confidence intervals (figure 14).
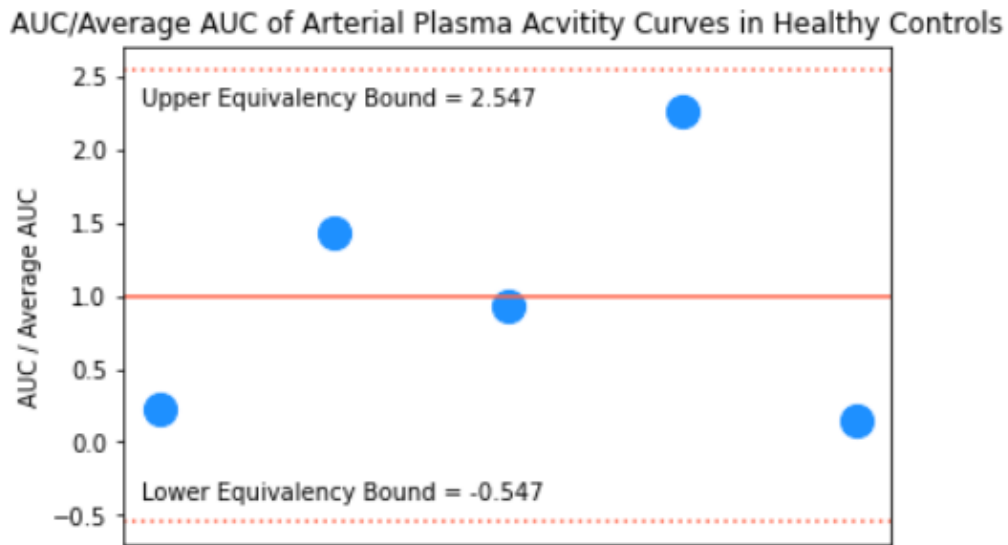

Figure 14: Establishing the equivalency bounds to be used in our venous groups by calculating the 95% confidence intervals in the arterial group. The standard deviation (stderr) of these five points is 0.789. The equivalency bounds are 1 +/- 1.96*stderr.

There are twice as many MA subjects as HC subjects, so when normalizing the AUC values, the contribution of each group had to be weighted accordingly. Ideally, this analysis would be performed with equal group sizes. The results are displayed in figure 15.
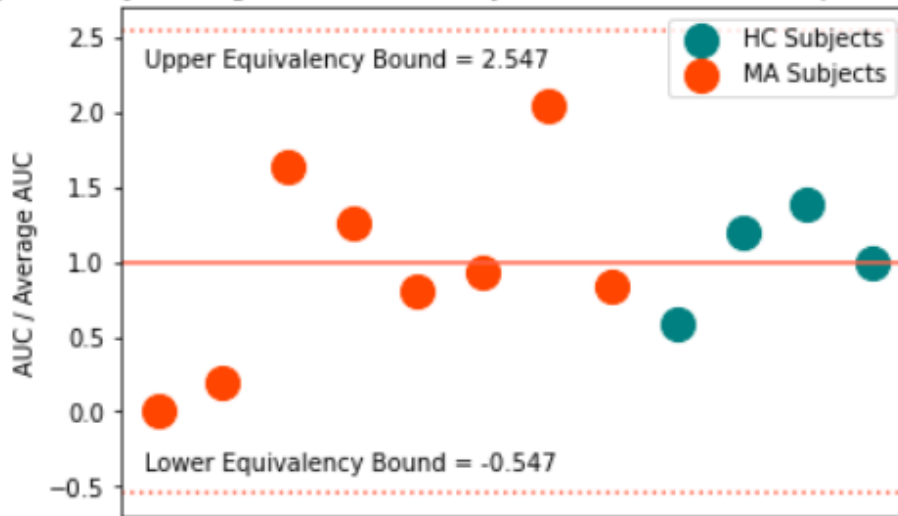
Figure 15: Equivalency testing the normalized plasma activity between MA users and healthy controls (HC). Equivalency bounds are set by the inter-subject variability seen in the HC atrial sampling group. All subjects from both groups fall within the equivalency bounds

All of the subjects fall within the equivalency bounds. This provides support to conclude that there are no effects large enough to be deemed clinically significant contributing to inherent differences between the two groups. From this, I conclude that there is no biological difference between the MA users and the HCs which significantly affects the levels of radiotracer within the plasma compartment. The predicted upregulation of PBR is not large enough to impact the concentration of blood tracer. This conclusion supports the decision to apply a PBIF generated using HC data to a group of MA data as a substitution for their arterial IF.

5.2 Comparison of V_T: Arterial IF Versus PBIF

All of the V_T comparison data are plotted in figures 16-18. When comparing the linear regression of the methods, ideally, the slope and the r-value approach one, and the y-intercept approaches zero. Figures 16-18 show that this is not reflected in all of the data sets, particularly with the PBIF which has undergone no scaling. When looking at the Krouwer plots, at least 95% of the data points need to be within the statistical bounds. Ideally, these bounds would be close

together to ensure that results are both statistically accurate and precise. To more easily visualize the values to be optimized, I plotted the differences from the ideal in 3x3 matrics representing the combinations of modeling and scaling techniques with scaled heatmapping (figure 19).

With the current dataset of processed subject visits, none of the modeling method and scaling technique combinations meet both the correlation and statistical agreement constraints set forth as evidence that a PBIF can be reliably used in place of an arterial IF. Of the quantification methods, SA resulted in the strongest correlations with r-values of 0.54, 0.96, and 0.8 when combined with different scaling techniques. The correlations resulting from CM and GA were very similar to each other. Predictably, not scaling the PBIF resulted in the worst correlations. The proposed novel scaling method based on BMI resulted in the highest correlations with r-values of 0.8 with SA and >0.9 with CM and GA.

Four combinations of modeling and scaling passed the criteria of having r-value >0.75 set for acceptance of correlation to move on to judging of statistical agreement. These were SA with blood scaling and BMI scaling, CM with BMI scaling, and GA with BMI scaling. Unfortunately, none of these combinations had 95% of their data points fall within the acceptable agreement intervals of the Krouwer plot. Of these, the combination of SA with blood scaling performed best with 88% of the data points falling into agreement bounds. The BMI scaling combinations had 70%, 69%, and 80% falling within agreement across the different modeling methods. The high correlations mean that the intervals are very narrow and so more data points will likely be required to reach significance. This analysis will need to be continued with more data points in order to confidently judge whether a generated PBIF can be used in an effort to not put subjects through arterial sampling.
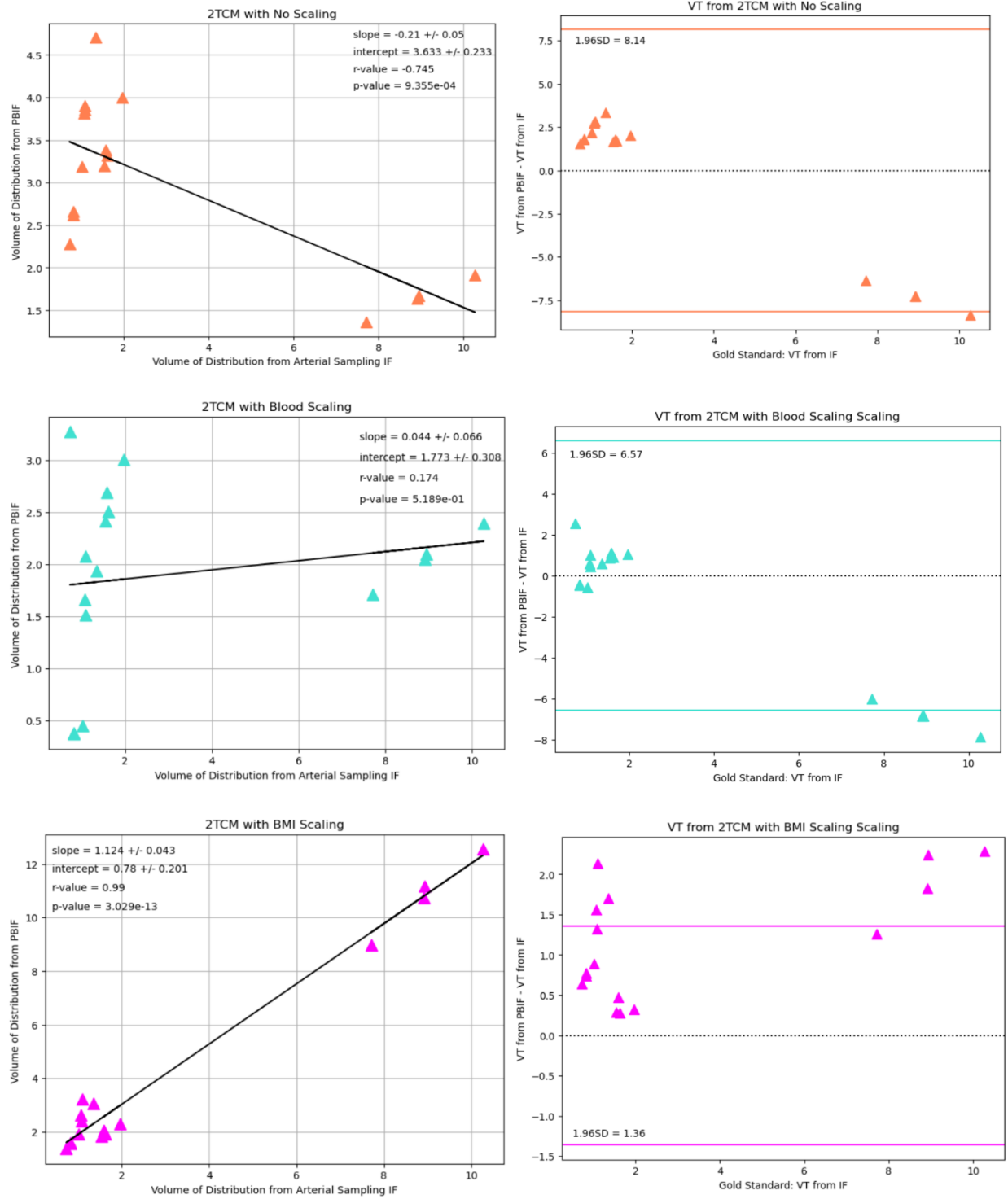
Figure 16: Method Comparison of arterial IF vs. PBIF using 2-tissue compartmental modeling. Each row shows a different scaling method (no scaling, blood activity scaling, BMI scaling). The left column employs a parametric least-squares linear regression. The right column uses the Krouwer modification of a Bland-Altman plot to test for statistical agreement.
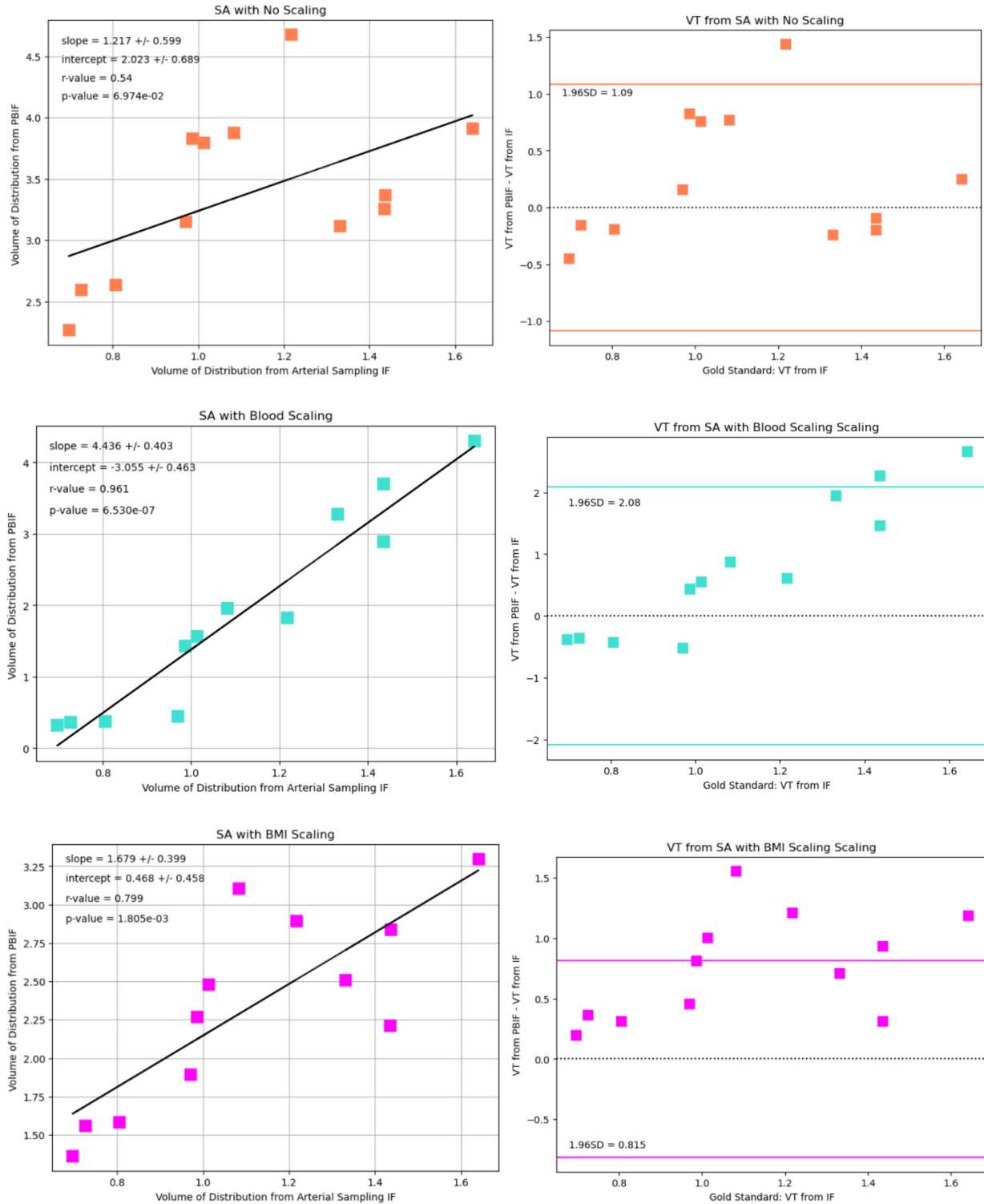
Figure 17: Method Comparison of arterial IF vs. PBIF using spectral analysis. Each row shows a different scaling method (no scaling, blood activity scaling, BMI scaling). The left column employs a parametric least-squares linear regression. The right column uses the Krouwer modification of a Bland-Altman plot to test for statistical agreement.
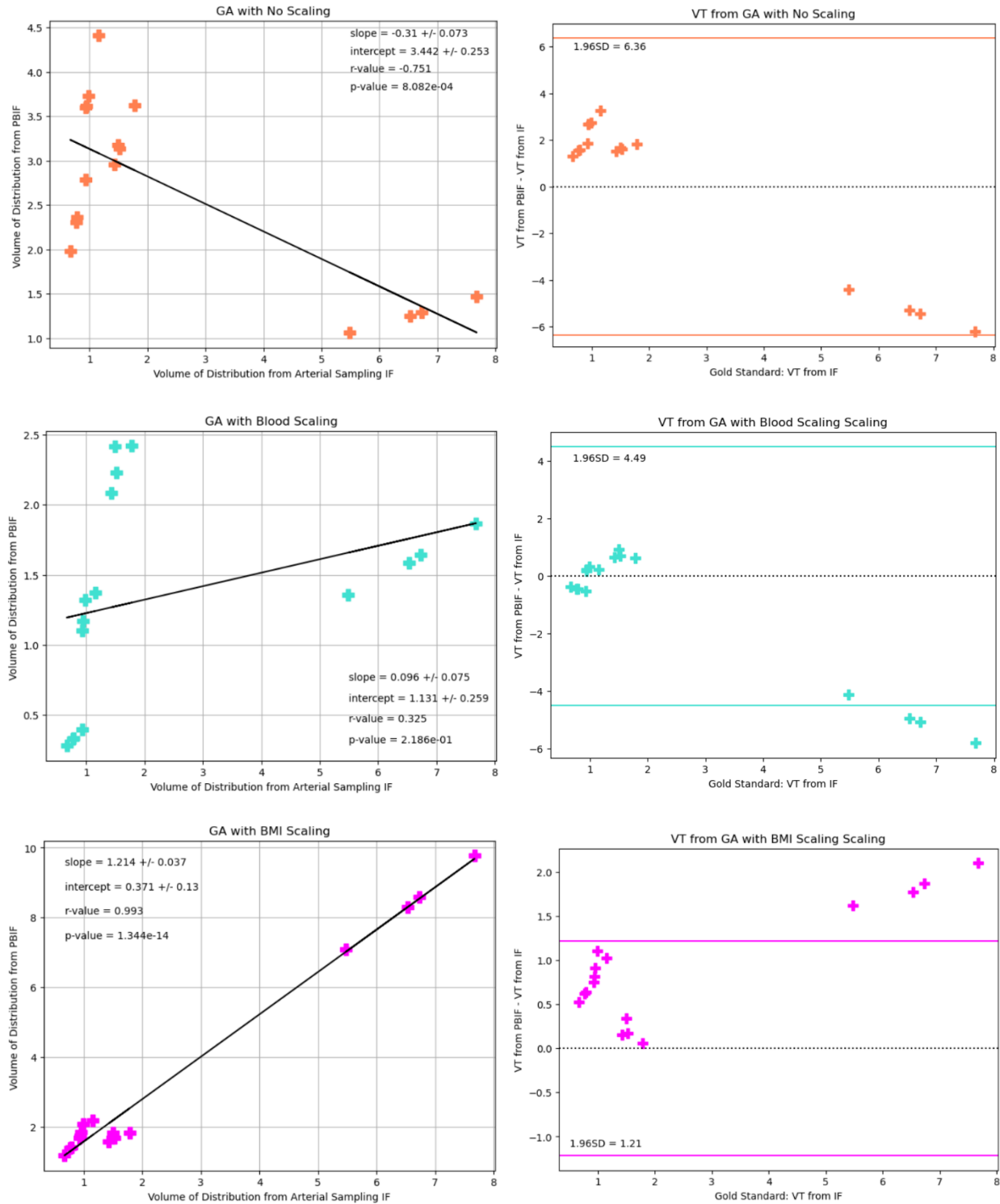
49

Figure 18: Method Comparison of arterial IF vs. PBIF using Logan graphical analysis. Each row shows a different scaling method (no scaling, blood activity scaling, BMI scaling). The left column employs a parametric least-squares linear regression. The right column uses the Krouwer modification of a Bland-Altman plot to test for statistical agreement.
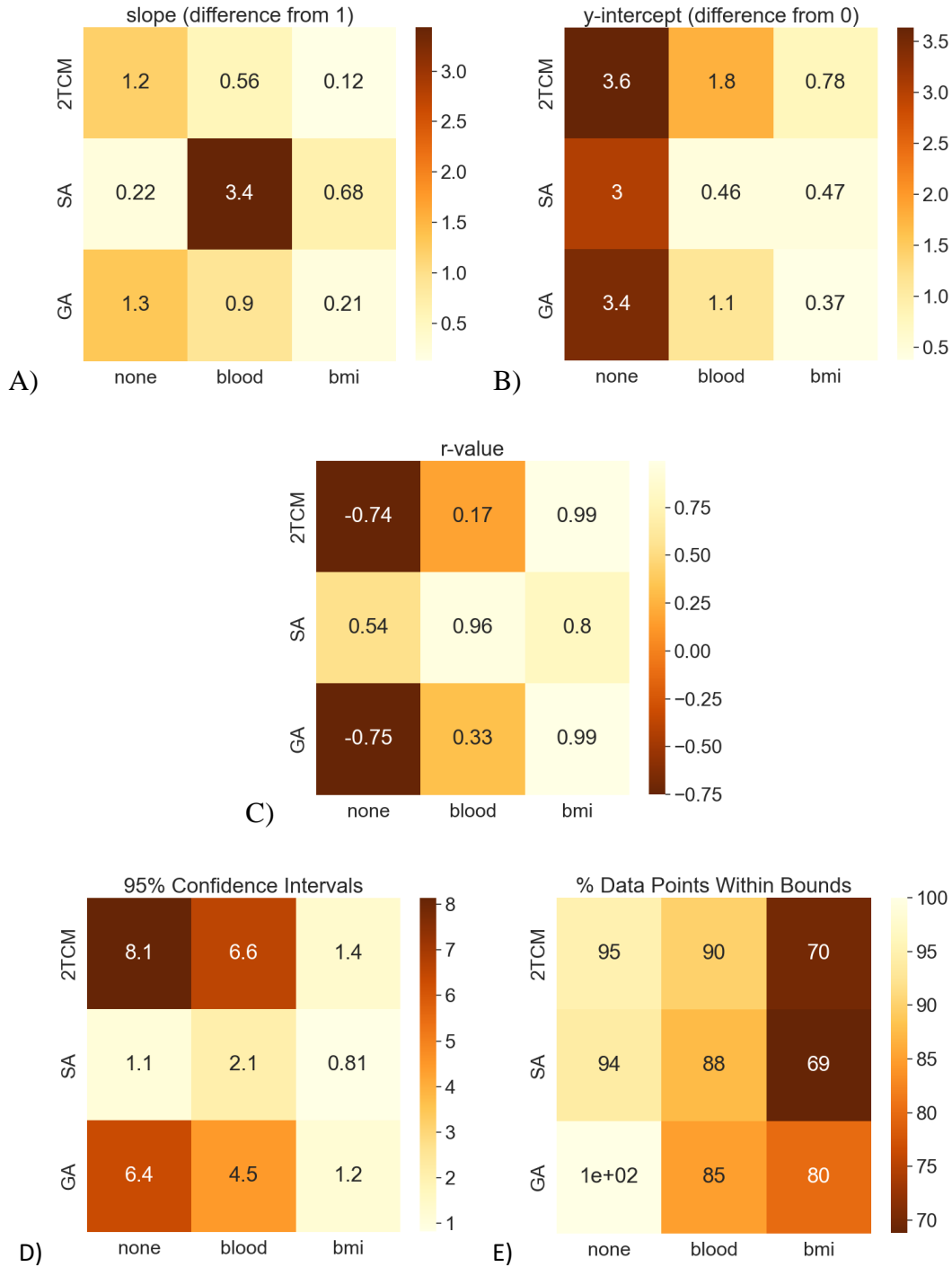
50

Figure 19: graphical representation with scaled heatmapping of the parameters which we use to judge the performance of each combination of modeling method and scaling technique. In all grids, lighter colors correspond to better performance. The first grids represent parameters obtained through plotting V_T obtained from use of arterial IF against V_T obtained from use of PBIF. The last two are parameters founds from the Krouwer plots. A) How different the slope is from 1. B) How different the y-intercept is from 0. C) The Pearson correlation coefficient. D) The +/- bounds set from the 95% confidence interval. E) The percentage of data points that fall within the agreement bounds

5.3 Limitations & Future Work

A significant limitation of this work is that arterial sampling was not collected from the MA group, thus limiting the ability to test with certainty that a PBIF is a suitable replacement for an arterial IF. A study performed last year compared modeling using venous blood samples against the gold standard of arterial blood samples in a [^{18}F]GE-179 PET study with promising results[68]. Investigation of venous modelling in [^{11}C]PBR28 studies would benefit this research study, however, it would require acquiring simultaneous venous and arterial samples from HC subjects.

Another major factor limiting our conclusions is the sample size. Recruiting during modified operations due to the global Covid-19 pandemic was challenging. Staffing constraints also made it difficult or impossible to set arterial lines in all of the HCs, further reducing the number of subjects we had available to generate and test the PBIF. PET scans have been acquired on more subjects since these analyses were performed and I intend to continue this work after the submission of the thesis and adding their data to the analysis. These new results may strengthen our agreement and increase our statistical power. Future directions also include creating and streamlining a workflow pipeline that enables future students or researchers in the group to continue processing the data and performing pharmacokinetic modeling in a similar manner. Our methods could be improved by a future student by implementing a CM that takes into account the vascular binding component. This thesis has laid the groundwork for future studies to continue to improve upon PET quantification in our cohort.

SUMMARY & CONCLUSIONS

This project explores the validity of using a PBIF for accurate [11C]PBR28 PET quantification which would do away with the need for invasive and risky arterial sampling in vulnerable populations, including IV drug users. Arterial sampling is not always possible due to its invasive nature and prohibitive staffing costs. A reliable alternative for use with [11C]PBR28 would expand scientific possibilities, allowing for the advancement of our understanding of the immunological responses associated with MUD and other diseases that present with neuroinflammation. The literature using image derived methods and pseudo-reference region methods as an alternative to arterial sampling in [11C]PBR28 studies show poor agreement results and limited reproducibility. PBIFs have been employed with different radiotracer studies with statistical success.

The first aim of this thesis was to determine whether a PBIF generated with HC arterial data can be applied to MA subjects. The statistical framework was based upon common statistical practices in the field of pharmacokinetics. Equivalency analysis of the MA users and the HCs revealed that there was no significant difference between the plasma concentrations of tracer in IV sampled blood between the two groups. This suggests that a PBIF constructed and validated in a HC group would be comparable to an IF generated with MA data and thus PBIF using controls can be applied to the MA group. This would be a significant contribution to the field and would limit the risk associated with arterial line placement in vulnerable populations.

The second aim therefore was to determine whether a PBIF from HC arterial plasma data would result in accurate quantification in an independent test group. Three different quantification methods were modeled to test whether a specific quantification method would perform more robustly when presented with differences in IF. Results from these three methods were similar, with SA slightly outperforming CM and GA. The PBIFs also needed to be scaled to account for intersubject variability. This was tested using the blood activity at a single time point and using the subject's BMI. Both scaling methods improved the results using a non-scaled PBIF. The BMI scaling method resulted in superior correlations with Pearson coefficients of 0.8 when using SA and >0.9 when using CM and Logan GA. Due to the small number of scans available for analysis in this thesis, none of the combinations of quantification method and PBIF scaling technique reached statistically significant agreement levels.

The strong correlations are promising that an accurately generated PBIF with a suitable scaling procedure could be used in place of arterial IFs in populations that are precluded from arterial cannulation. However, more HC subjects' scans would need to be added to our analysis in order to strengthen the agreement statistics before any substitution is implemented into practice. As patients' scans are currently ongoing in this study, it should be possible to expand our analysis and make more definitive conclusions.

In order to obtain rigorous quantification of neuroinflammation levels in the MA group, a validated alternative to arterial IFs is imperative. A mechanistic understanding of the effect of neuroinflammation in MUD and its treatment could dramatically improve the lives of the millions of people suffering from this neuropsychiatric disorder and also relieve a significant public health burden.

REFERENCES

1. Winkelman TNA, Admon LK, Jennings L, Shippee ND, Richardson CR, Bart G. Evaluation of Amphetamine-Related Hospitalizations and Associated Clinical Outcomes and Costs in the United States. *JAMA Netw Open*. 2018;1(6):e183758-e183758. doi:10.1001/jamanetworkopen.2018.3758

2. Melega WP, Raleigh MJ, Stout DB, Lacan G, Huang SC, Phelps ME. Recovery of striatal dopamine function after acute amphetamine- and methamphetamine-induced neurotoxicity in the vervet monkey. *Brain Res*. Aug 22 1997;766(1-2):113-20. doi:10.1016/s0006-8993(97)00548-9

3. Rathitharan G, Truong J, Tong J, et al. Microglia imaging in methamphetamine use disorder: a positron emission tomography study with the 18 kDa translocator protein radioligand [F-18]FEPPA. *Addict Biol*. Jan 2021;26(1):e12876. doi:10.1111/adb.12876

4. London ED, Kohno M, Morales AM, Ballard ME. Chronic methamphetamine abuse and corticostriatal deficits revealed by neuroimaging. *Brain Res*. Dec 2 2015;1628(Pt A):174-85. doi:10.1016/j.brainres.2014.10.044

5. Li MJ, Briones MS, Heinzerling KG, Kalmin MM, Shoptaw SJ. Ibudilast attenuates peripheral inflammatory effects of methamphetamine in patients with methamphetamine use disorder. *Drug Alcohol Depend*. Jan 1 2020;206:107776. doi:10.1016/j.drugalcdep.2019.107776

6. Wang A, Hendin A, Millington SJ, Koenig S, Eisen LA, Shiloh AL. Better With Ultrasound: Arterial Line Placement. *Chest*. Mar 2020;157(3):574-579. doi:10.1016/j.chest.2019.08.2209

7. Agarwal K, Manza P, Chapman M, et al. Inflammatory Markers in Substance Use and Mood Disorders: A Neuroimaging Perspective. *Front Psychiatry*. 2022;13:863734. doi:10.3389/fpsyt.2022.863734

8. Mijnarends PE. Determination of Anisotropic Momentum Distributions in Positron Annihilation. *Physical Review*. 08/15/ 1967;160(3):512-519. doi:10.1103/PhysRev.160.512

9. Bushberg JT. *The essential physics of medical imaging*. Wolters Kluwer / Lippincott Williams & Wilkins; 2012.

10. Lecoq P. Scintillation Detectors for Charged Particles and Photons. In: Fabjan CW, Schopper H, eds. *Particle Physics Reference Library: Volume 2: Detectors for Particles and Radiation*. Springer International Publishing; 2020:45-89.

11. Dimitrakopoulou-Strauss A, Pan L, Sachpekidis C. Kinetic modeling and parametric imaging with dynamic PET for oncological applications: general considerations, current clinical applications, and future perspectives. *European Journal of Nuclear Medicine and Molecular Imaging*. 2021/01/01 2021;48(1):21-39. doi:10.1007/s00259-020-04843-6

12. Kiebel SJ, Ashburner J, Poline J-B, Friston KJ. MRI and PET Coregistration—A Cross Validation of Statistical Parametric Mapping and Automated Image Registration. *NeuroImage*. 1997/05/01/ 1997;5(4):271-279. doi:https://doi.org/10.1006/nimg.1997.0265

13. Zhang Y, Fox GB. PET imaging for receptor occupancy: meditations on calculation and simplification. *J Biomed Res*. 2012;26(2):69-76. doi:10.1016/S1674-8301(12)60014-1

14. Gjedde A, Bauer W, Wong DF. *Neurokinetics: The dynamics of neurobiology in vivo*. Springer US; 2011.

15. Kimura Y, Naganawa M, Sakata M, et al. Distribution volume as an alternative to the binding potential for sigma1 receptor imaging. *Annals of Nuclear Medicine*. 2007/11/01 2007;21(9):533-535. doi:10.1007/s12149-007-0063-6

16. Kimura Y, Naganawa M, Sakata M, et al. Distribution volume as an alternative to the binding potential for sigma1 receptor imaging. *Ann Nucl Med*. Nov 2007;21(9):533-5. doi:10.1007/s12149-007-0063-6

17. Gavish M, Bachman I, Shoukrun R, et al. Enigma of the peripheral benzodiazepine receptor. *Pharmacol Rev*. Dec 1999;51(4):629-50.

18. Jayakumar AR, Panickar KS, Norenberg MD. Effects on free radical generation by ligands of the peripheral benzodiazepine receptor in cultured neural cells. *J Neurochem*. Dec 2002;83(5):1226-34. doi:10.1046/j.1471-4159.2002.01261.x

19. Rizzo G, Veronese M, Tonietto M, et al. Generalization of endothelial modelling of TSPO PET imaging: Considerations on tracer affinities. *J Cereb Blood Flow Metab*. May 2019;39(5):874-885. doi:10.1177/0271678x17742004

20. Rizzo G, Veronese M, Tonietto M, Zanotti-Fregonara P, Turkheimer FE, Bertoldo A. Kinetic modeling without accounting for the vascular component impairs the quantification of [(11)C]PBR28 brain PET data. *J Cereb Blood Flow Metab*. Jun 2014;34(6):1060-9. doi:10.1038/jcbfm.2014.55

21. Turkheimer FE, Rizzo G, Bloomfield PS, et al. The methodology of TSPO imaging with positron emission tomography. *Biochem Soc Trans*. Aug 2015;43(4):586-92. doi:10.1042/bst20150058

22. James ML, Selleri S, Kassiou M. Development of ligands for the peripheral benzodiazepine receptor. *Curr Med Chem*. 2006;13(17):1991-2001. doi:10.2174/092986706777584979

23. Hu X, Liou AK, Leak RK, et al. Neurobiology of microglial action in CNS injuries: receptor-mediated signaling mechanisms and functional roles. *Prog Neurobiol*. Aug-Sep 2014;119-120:60-84. doi:10.1016/j.pneurobio.2014.06.002

24. Venneti S, Lopresti BJ, Wiley CA. The peripheral benzodiazepine receptor (Translocator protein 18kDa) in microglia: from pathology to imaging. *Prog Neurobiol*. Dec 2006;80(6):308-22. doi:10.1016/j.pneurobio.2006.10.002

25. Albrecht DS, Granziera C, Hooker JM, Loggia ML. In Vivo Imaging of Human Neuroinflammation. *ACS Chem Neurosci*. Apr 20 2016;7(4):470-83. doi:10.1021/acschemneuro.6b00056

26. MacAskill MG, Stadulyte A, Williams L, et al. Quantification of Macrophage-Driven Inflammation During Myocardial Infarction with (18)F-LW223, a Novel TSPO Radiotracer with Binding Independent of the rs6971 Human Polymorphism. *J Nucl Med*. Apr 2021;62(4):536-544. doi:10.2967/jnumed.120.243600

27. Berroterán-Infante N, Kalina T, Fetty L, et al. (R)-[(18)F]NEBIFQUINIDE: A promising new PET tracer for TSPO imaging. *Eur J Med Chem*. Aug 15 2019;176:410-418. doi:10.1016/j.ejmech.2019.05.008

28. Briard E, Zoghbi SS, Imaizumi M, et al. Synthesis and evaluation in monkey of two sensitive 11C-labeled aryloxyanilide ligands for imaging brain peripheral benzodiazepine receptors in vivo. *J Med Chem*. Jan 10 2008;51(1):17-30. doi:10.1021/jm0707370

29. Tu Z, Mach RH. C-11 radiochemistry in cancer imaging applications. *Curr Top Med Chem*. 2010;10(11):1060-95. doi:10.2174/156802610791384261

30. Chiou WL. The phenomenon and rationale of marked dependence of drug concentration on blood sampling site. Implications in pharmacokinetics, pharmacodynamics, toxicology and therapeutics (Part I). *Clin Pharmacokinet*. Sep 1989;17(3):175-99. doi:10.2165/00003088-198917030-00004

31. Chiou WL. *The Phenomenon and Rationale of Marked Dependence of Drug Concentration on Blood Sampling Site*.

32. Akizawa H, Uehara T, Arano Y. Renal uptake and metabolism of radiopharmaceuticals derived from peptides and proteins. *Adv Drug Deliv Rev*. Sep 2008;60(12):1319-28. doi:10.1016/j.addr.2008.04.005

33. Datta G, Colasanti A, Kalk N, et al. (11)C-PBR28 and (18)F-PBR111 Detect White Matter Inflammatory Heterogeneity in Multiple Sclerosis. *J Nucl Med*. Sep 2017;58(9):1477-1482. doi:10.2967/jnumed.116.187161

34. Lyoo CH, Ikawa M, Liow JS, et al. Cerebellum Can Serve As a Pseudo-Reference Region in Alzheimer Disease to Detect Neuroinflammation Measured with PET Radioligand Binding to Translocator Protein. *J Nucl Med*. May 2015;56(5):701-6. doi:10.2967/jnumed.114.146027

35. Nair A, Veronese M, Xu X, et al. Test-retest analysis of a non-invasive method of quantifying [(11)C]-PBR28 binding in Alzheimer's disease. *EJNMMI Res*. Dec 2016;6(1):72. doi:10.1186/s13550-016-0226-3

36. Krejza J, Arkuszewski M, Kasner SE, et al. Carotid artery diameter in men and women and the relation to body and neck size. *Stroke*. Apr 2006;37(4):1103-5. doi:10.1161/01.STR.0000206440.48756.f7

37. Zanotti-Fregonara P, Liow JS, Fujita M, et al. Image-derived input function for human brain using high resolution PET imaging with [C](R)-rolipram and [C]PBR28. *PLoS One*. Feb 25 2011;6(2):e17056. doi:10.1371/journal.pone.0017056

38. Aceves-Serrano L, Sossi V, Doudet DJ. Comparison of Invasive and Non-invasive Estimation of [(11)C]PBR28 Binding in Non-human Primates. *Mol Imaging Biol*. Oct 7 2021;doi:10.1007/s11307-021-01661-6

39. Naganawa M, Gallezot JD, Shah V, et al. Assessment of population-based input functions for Patlak imaging of whole body dynamic (18)F-FDG PET. *EJNMMI Phys*. Nov 23 2020;7(1):67. doi:10.1186/s40658-020-00330-x

40. Zanotti-Fregonara P, Hines CS, Zoghbi SS, et al. Population-based input function and image-derived input function for [¹¹C](R)-rolipram PET imaging: methodology, validation and application to the study of major depressive disorder. *Neuroimage*. Nov 15 2012;63(3):1532-41. doi:10.1016/j.neuroimage.2012.08.007

41. Akerele MI, Zein SA, Pandya S, et al. Population-based input function for TSPO quantification and kinetic modeling with [(11)C]-DPA-713. *EJNMMI Phys*. Apr 29 2021;8(1):39. doi:10.1186/s40658-021-00381-8

42. Thie JA. Understanding the standardized uptake value, its methods, and implications for usage. *J Nucl Med*. Sep 2004;45(9):1431-4.

43. Keyes JW, Jr. SUV: standard uptake or silly useless value? *J Nucl Med*. Oct 1995;36(10):1836-9.

44. Huang S-C. Anatomy of SUV. *Nuclear Medicine and Biology*. 2000/10/01/ 2000;27(7):643-646. doi:https://doi.org/10.1016/S0969-8051(00)00155-4

45. Hamberg LM, Hunter GJ, Alpert NM, Choi NC, Babich JW, Fischman AJ. The dose uptake ratio as an index of glucose metabolism: useful parameter or oversimplification? *J Nucl Med*. Aug 1994;35(8):1308-12.

46. Watabe H, Ikoma Y, Kimura Y, Naganawa M, Shidahara M. PET kinetic analysis--compartmental model. *Ann Nucl Med*. Nov 2006;20(9):583-8. doi:10.1007/bf02984655

47. Willems JC. From time series to linear system—Part I. Finite dimensional linear time invariant systems. *Automatica*. 1986/09/01/ 1986;22(5):561-580. doi:https://doi.org/10.1016/0005-1098(86)90066-X

48. Veronese M, Rizzo G, Bertoldo A, Turkheimer FE. Spectral Analysis of Dynamic PET Studies: A Review of 20 Years of Method Developments and Applications. *Comput Math Methods Med*. 2016;2016:7187541. doi:10.1155/2016/7187541

49. Veronese M, Rizzo G, Turkheimer FE, Bertoldo A. SAKE: a new quantification tool for positron emission tomography studies. *Comput Methods Programs Biomed*. Jul 2013;111(1):199-213. doi:10.1016/j.cmpb.2013.03.016

50. Cunningham VJ, Jones T. Spectral analysis of dynamic PET studies. *J Cereb Blood Flow Metab*. Jan 1993;13(1):15-23. doi:10.1038/jcbfm.1993.5

51. Pmod. PMOD Kinetic Modeling Tool (PKIN).

52. Zhou Y, Ye W, Brasić JR, Wong DF. Multi-graphical analysis of dynamic PET. *Neuroimage*. Feb 15 2010;49(4):2947-57. doi:10.1016/j.neuroimage.2009.11.028

53. Logan J, Fowler JS, Volkow ND, Wang GJ, Ding YS, Alexoff DL. Distribution volume ratios without blood sampling from graphical analysis of PET data. *J Cereb Blood Flow Metab*. Sep 1996;16(5):834-40. doi:10.1097/00004647-199609000-00008

54. Kimura Y, Naganawa M, Shidahara M, Ikoma Y, Watabe H. PET kinetic analysis --pitfalls and a solution for the Logan plot. *Ann Nucl Med*. Jan 2007;21(1):1-8. doi:10.1007/bf03033993

55. Yoder KK, Territo PR, Hutchins GD, et al. Comparison of standardized uptake values with volume of distribution for quantitation of [(11)C]PBR28 brain uptake. *Nucl Med Biol*. Mar 2015;42(3):305-8. doi:10.1016/j.nucmedbio.2014.11.003

56. Zanotti-Fregonara P, Kreisl WC, Innis RB, Lyoo CH. Automatic Extraction of a Reference Region for the Noninvasive Quantification of Translocator Protein in Brain Using (11)C-PBR28. *J Nucl Med*. Jul 2019;60(7):978-984. doi:10.2967/jnumed.118.222927

57. Paul S, Gallagher E, Liow JS, et al. Building a database for brain 18 kDa translocator protein imaged using [(11)C]PBR28 in healthy subjects. *J Cereb Blood Flow Metab*. Jun 2019;39(6):1138-1147. doi:10.1177/0271678x18771250

58. Martin Paulus M. Methamphetamine use disorder: Epidemiology, clinical features, and diagnosis. https://www.uptodate.com/contents/methamphetamine-use-disorder-epidemiology-clinical-features-and-diagnosis

59. Anglin MD, Burke C, Perrochet B, Stamper E, Dawud-Noursi S. History of the methamphetamine problem. *J Psychoactive Drugs*. Apr-Jun 2000;32(2):137-41. doi:10.1080/02791072.2000.10400221

60. Tonietto M, Veronese M, Rizzo G, et al. Improved models for plasma radiometabolite correction and their impact on kinetic quantification in PET studies. *J Cereb Blood Flow Metab*. Sep 2015;35(9):1462-9. doi:10.1038/jcbfm.2015.61

61. Buchert R, Dirks M, Schütze C, et al. Reliable quantification of (18)F-GE-180 PET neuroinflammation studies using an individually scaled population-based input function or late tissue-to-blood ratio. *Eur J Nucl Med Mol Imaging*. Nov 2020;47(12):2887-2900. doi:10.1007/s00259-020-04810-1

62. Banks WA. Characteristics of compounds that cross the blood-brain barrier. *BMC Neurol*. Jun 12 2009;9 Suppl 1(Suppl 1):S3. doi:10.1186/1471-2377-9-s1-s3

63. Pmod. PMOD Neuro Tool (PNEURO) User Manual Version 4.3. https://doc.pmod.com/PDF/PNEURO.pdf

64. Hammers A, Allom R, Koepp MJ, et al. Three-dimensional maximum probability atlas of the human brain, with particular reference to the temporal lobe. *Hum Brain Mapp*. Aug 2003;19(4):224-47. doi:10.1002/hbm.10123

65. Hauck WW, Anderson S. A new statistical procedure for testing equivalence in two-group comparative bioavailability trials. *J Pharmacokinet Biopharm*. Feb 1984;12(1):83-91. doi:10.1007/bf01063612

66. Bland JM, Altman DG. Statistical methods for assessing agreement between two methods of clinical measurement. *Lancet*. Feb 8 1986;1(8476):307-10.

67. Krouwer JS. Why Bland-Altman plots should use X, not (Y+X)/2 when X is a reference method. *Stat Med*. Feb 28 2008;27(5):778-80. doi:10.1002/sim.3086

68. Galovic M, Erlandsson K, Fryer TD, et al. Validation of a combined image derived input function and venous sampling approach for the quantification of [(18)F]GE-179 PET binding in the brain. *Neuroimage*. Aug 15 2021;237:118194. doi:10.1016/j.neuroimage.2021.118194